Angewandte Chemie
Eine Zeitschrift der Gesellschaft Deutscher Chemiker

Supporting Information

Unlocking Mesoscopic Disorder in Graphitic Carbon with Spectroelectrochemistry

*R. Papadopoulos, B. Masters, A. Kundu, N. Maldonado, A. S. Filatov, Y. Liu, T. Kim, G. Galli, A. Wuttig**

Supporting Information

Unlocking Mesoscopic Disorder in Graphitic Carbon with Spectroelectrochemistry

Ry Papadopoulos,[1,+] Benjamin Masters,[1,+] Arpan Kundu,[1,2,+] Nicholas Maldonado,[1] Alexander S. Filatov,[1] Yuzi Liu,[3] Taemin Kim,[1] Giulia Galli,[1,2,3] Anna Wuttig[1,*]

[1]Department of Chemistry, University of Chicago, Chicago, IL, 60637, United States

[2]Pritzker School of Molecular Engineering, University of Chicago, Chicago, IL, 60637, United States

[3]Argonne National Laboratory, Lemont, IL, 60439, United States

Corresponding author: awuttig@uchicago.edu

Table of Contents

Experimental Procedures

1. General Methods. Reagents were purchased from commercial sources and used without further purification unless otherwise noted. Dichloromethane (CH_2Cl_2) was dried and purified using a solvent purification system (PureSolv MD 5, INERT Corporation) under N_2.

2. Electrochemical Methods. Electrochemical experiments were conducted using a Gamry Reference 620 Potentiostat, a Ag/AgCl reference electrode (eDAQ, leakless), a high surface area Pt-mesh counter electrode (Alfa Aesar, 99.997 %), and various working electrodes. The Ag/AgCl electrode was stored in Millipore Type 1, 18.2 MΩ, water between measurements and was periodically checked relative to a pristine Ag/AgCl electrode to ensure against potential drift. All experiments were performed at 21±1 ℃. Electrode potentials reported are referenced against the RHE standard using the conversion, $E_{\text{V vs. Ag/AgCl}} + 0.205\ \text{V} + (0.059*\text{pH}) = E_{\text{V vs. RHE}}$. Current density values are reported relative to the geometric surface area of the working electrode. An electrochemical cell was utilized and held 10 mL of electrolyte (James Glass Inc.) to prepare samples used to construct **Figures 1b and 1d-f, S1-4, S7**, red, **S8**, grey, **S12, S14, 15**. Otherwise, a spectroelectrochemical cell (PIKE Jackfish J2) was used to prepare samples used to construct **Figures 1a and 1c, 2, S6,** grey, **S9-10, S13, S16-23**. Cyclic voltammograms were processed using Origin software. FFT filters were used with point of window = 15. **Figure S3** uses a glassy carbon foil (Goodfellow) with an area of ~ 0.5 cm^2 as the working electrode.

3. Synthesis of Au Films on Si. Au films were prepared on undoped Si prisms (PIKE, face-angled crystal) using the "double deposition method" as previously detailed.[1,2] The geometric surface area of the SEIRAS film exposed to the electrolyte was 0.71 cm^2. Following the deposition, the Au-coated Si prism was assembled into a spectroelectrochemical cell (PIKE Jackfish J2) and cleaned using an electrochemical procedure. The film was cycled in 0.1 M H_2SO_4 from 0.10 V vs. Ag/AgCl to 1.50 V vs. Ag/AgCl at 50 mV s^{-1} for 10 consecutive cycles. Following, the 0.1 M H_2SO_4 was replaced with MilliQ water, and the film was washed 3 to 5 times with MilliQ water. For *ex-situ* experiments that cannot accommodate the Si prism size, Au films were prepared on an N-type Flat Zone (FZ) Si wafer (WaferPro) using the same "double deposition method" as previously detailed.[1,2] The geometric surface area of the wafers varied from 0.25 to 1.5 cm^2.

4. Electrodeposition procedure of reduced graphene oxide (rGO) on Au-coated Si prisms (4.1), Si wafers (4.2), Au Disk (4.3), or evaporated Au substrates on aluminosilicate glass slides (4.4).

4.1 Electrodeposition procedure of rGO on Au-coated Si prisms. This procedure was used to make the rGO substrates in **Figures 1a, and 1c, 2, S6,** black**, S9, S10,** and **S16-23**. A 2 mg/mL graphene oxide (GO) dispersion was purchased and used without further purification (Sigma Aldrich). A solution of 1 mg/mL GO and 0.1 M $NaNO_3$ (Thermo Scientific, >99.99% trace metals basis) was prepared by making 5 mL of 0.2 M $NaNO_3$ in MilliQ water and combining with 5 mL of the 2 mg/mL GO dispersion.[3] The combined solution was ultrasonicated for 30 min prior to use in an electrochemical cell to improve the dispersibility of the GO in water. In parallel, Au films were deposited on a Si prism using the method described in Section 3 above. Additionally, before the introduction of GO, the Au film was cycled in 0.1 M H_2SO_4 from 0.10 V vs. Ag/AgCl to 1.50 V vs. Ag/AgCl at 100 mV s^{-1} for 10 consecutive cycles. Following, the 0.1 M H_2SO_4 was replaced with MilliQ water, and the film was rinsed 3 to 5 times. Next, the prepared GO and $NaNO_3$ solution was added to the electrochemical cell with the Au working electrode, Ag/AgCl reference electrode, and a Pt-mesh counter electrode. An initial 3-cycle cyclic voltammogram of this solution was taken from 0.3 V vs Ag/AgCl to –1.2 V vs Ag/AgCl at 100 mV s^{-1} (see **Figure S1b** for a representative cyclic voltammogram taken using Au disk instead of Au film on Si prism). Immediately following, a constant potential electrolysis at –1.1 V vs Ag/AgCl of the GO and $NaNO_3$ is performed while stirring or bubbling N_2 for 2-10 min for a thin film, and 60-90 minutes for a thick film (the time depends on the sample area in order to achieve full rGO coverage, see **Figure S1c** for a representative chronoamperometry trace taken using Au disk instead of Au film on Si prism). Following electrolysis, the newly deposited rGO was gently

washed with MilliQ water and heated at 60°C for 20 min. The absence of exposed Au was tested by the observation of the suppression of the hydrogen evolution reaction (HER) relative to bare Au and identical to glassy carbon electrodes (see **Figure S3** for a representative cyclic voltammogram taken using Au foil instead of Au film on Si prism). HER of the rGO/Au-coated Si was performed in a 0.1 M pH 7.4 sodium phosphate (NaP_i) buffer using sodium phosphate dibasic (Sigma Aldrich, >99.0%) and sodium phosphate monobasic (Sigma Aldrich, > 98.0%) or in 0.1 M pH 7 sodium chloride (NaCl) (Sigma Aldrich, >99.0%) to rule out effects of phosphates. Cyclic voltammograms were scanned from 0 V vs Ag/AgCl to –1.2 V vs Ag/AgCl. Typical HER suppression is compared with a glassy carbon disk electrode (CH instruments, 3 mm diameter), shown in **Figure S3**. Prior to use, the glassy carbon electrode was polished for 3 min in 1 μm alumina polish and sonicated for 5 min in MilliQ.

4.2 Electrodeposition procedure of rGO on Au-coated Si wafers. This procedure was used to make the rGO substrates in **Figures 1b, 1d-e**, **S4, S12** due to instrument height constraints. Following the same GO solution preparation outlined in Section 4.1, above, the Au film was deposited on a Si wafer using the method described in Section 3 above. Electrochemical contact was established using a stainless-steel clip that made direct contact with the Au surface. Additionally, before the introduction of GO, the Au surface was cycled in H_2SO_4, and washed, and GO was electrochemically reduced onto the Au surface using the same procedure outlined in Section 4.1.

4.3 Electrodeposition procedure of rGO on Au disk and foil electrodes. This procedure was used to make the rGO substrates in **Figure S1** (disk) and **Figures S3** (foil) due to cell geometry constraints. In parallel with the same GO solution preparation outlined in Section 4.1, above, the Au disk electrode (DE, from CH Instruments, 0.0314 cm^2) or Au foil electrode (Alfa Aesar) was polished for 3 min in 1 μm alumina polish and sonicated for 5 min in MilliQ. Additionally, before the introduction of GO, the Au disk or foil electrode was cycled in H_2SO_4, and washed, and GO was electrochemically reduced onto the Au surface using the same procedure outlined in Section 4.1. The area of the Au foil electrode was about 2 cm^2.

4.4 Electrodeposition procedure of rGO on evaporated Au substrates on aluminosilicate glass slide. This procedure was used to make the rGO substrates in **Figures 1f**, **S14** and **S15**. With the same GO solution preparation outlined in Section 4.1, above, the evaporated Au on aluminosilicate glass slide (Sigma Aldrich, Product Number: 643246) was cycled in H_2SO_4 and washed, and GO was electrochemically reduced onto the Au surface. Electrochemical contact was established using a stainless-steel clip that made direct contact with the Au surface. Thick rGO was deposited for **Figure 1f** to obtain a strong signal and rule out a broad XRD feature resulting from a film with nanometer-scale thickness. A thick rGO film was also deposited for **Figures S14** and **S15** to minimize the signal from the underlying substrate. The heights of the thicker films were characterized by profilometry (see Section 7).

5. Atomic Force Microscopy. Step height and morphological studies on rGO/Au and Au were imaged using atomic force microscopy (AFM). All measurements were conducted on the Bruker Multimode 8 AFM in standard tapping mode using a Silicon cantilever (AppNano ACTA, radius of 6 nm, spring constant of 37 N/m, resonance frequency of 300 kHz, Olympus). AFM studies were conducted using Si wafers instead of Si prisms to account for the height requirements of the instrument as noted in Section 4.2.

6. Raman Spectroscopy. All Raman spectra were collected on a HORIBA LabRAM HR Evolution Confocal Raman Microscope with a 532 nm laser excitation source, and a Horiba Synapse OE-CCD detector. Raman spectra were taken with a Si(111) calibration standard at 520 cm^{-1} with a spectral resolution of 0.3 cm^{-1} and a 50x objective for all samples. GO samples were drop-cast (2 mg/mL solution, Sigma Aldrich) onto a Au-coated Si wafer (see Section 4) and dried under a stream of N_2. rGO was deposited on an Au-coated Si prism as described in Section 4.2.

7. Profilometry Measurements. Profilometry measurements were performed using an Olympus OLS5000 LEXT equipped with a MPLAON100xLEXT lens. The instrument was used in the 3D Fine + Color scanning mode.

8. Attenuated Total Reflection Infrared Absorption Spectroscopy (ATR-IR). All IR spectra were recorded in an attenuated total reflection (ATR) configuration using a Nicolet iS50 FTIR spectrometer equipped with a HgCdTe (MCT) detector (Ref/02 Gain Setting) and a PIKE VeeMax III accessory (incident angle of 30˚ with respect to normal). The Nicolet spectrometer was operated in series mode with an optical velocity of 1.8988 cm s^{-1}. All ATR-IR spectra are reported in absorbance units defined as $A=-\log(I/I_0)$, where I and I_0 stand for the sample and reference single-beam spectra, respectively. The PIKE Jackfish J2 spectroelectrochemical cells were used with undoped Si prisms (PIKE, face angled crystal). Data analyses were conducted using the OMNIC version 9.12.928 software. Peak positions from **Figures 2c, S19, and S22** reported in **Tables S5, S6, and S8** are the local maxima in the ranges of 1650-1500 cm^{-1} and 1400-1200 cm^{-1}. For **Figures 2** and **S18-23**, spectra were sequentially acquired with a spectral resolution of 4 cm^{-1} at every 19.2(8) s interval.

9. ATR-IR Measurements Performed *Ex-Situ*. Spectra were recorded on a Thermo Nicolet iS50 Advanced FTIR equipped with an MCT-A detector, using a PIKE VeeMax III accessory (incident angle of 30˚ with respect to normal). The sample was placed on the ATR crystal and spectra were taken with a spectral resolution of 4 cm^{-1} and a single beam spectrum (32 scans) loaded as a background (**Figures S7 and S8**).

10. IR of 4-nitrobenzoic acid on Au, rGO/Au, and Si. 4-nitrobenzoic acid (Sigma Aldrich, 98%) was used. A concentrated stock solution was made of 3.53 mM 4-nitrobenzoic acid in 10 mL $CHCl_3$ (Fisher Scientific) and a serial dilution was undertaken on this solution to obtain two separate solutions of 0.353 mM and 0.0353 mM in $CHCl_3$. The ATR-IR optical configuration follows the procedures outlined in Section 8. Prior to background collection, 5 μL of $CHCl_3$ was placed onto the surface of the material and dried under a stream of N_2. Thus, the background for Si (**Figures S16 and S17**, black) is the bare Si prism after drying $CHCl_3$ from its surface; the background for Au (**Figures S16,** red, **and S17**, blue) is the bare, dry Au-coated Si prism after drying $CHCl_3$ from its surface, and the background for rGO on Au-coated Si prism (**Figures S16,** blue**, and S17**, red) is the bare, dry rGO film after drying $CHCl_3$ from its surface. Following, 5 μL of 0.0353 mM 4-nitrobenzoic acid was initially dropcast on the surface and the $CHCl_3$ was evaporated before taking an ATR-IR spectrum. Following, increasing amounts of 4-nitrobenzoic acid were added following the same drop casting procedure to obtain **Figure S16**. Error bars (**Figure S16**) represent the standard deviation from the average integrated signal intensity of three independent runs on each surface type (bare Si, Au-coated Si, and rGO on Au-coated Si).

11. X-ray Photoelectron Spectroscopy. X-ray photoelectron spectroscopy (XPS) measurements were collected on an as-prepared nanostructured Au or rGO/Au-coated Si prism (see Sections 3 and 4, above). XPS samples were prepared by adhering the prisms to the sample stage with carbon tape connected to the Au portion of the surface of the prism and transferred to the ultra-high vacuum chamber. The X-ray photoelectron spectra were collected using an AXIS Nova spectrometer (Kratos Analytical) equipped with a monochromatic Al Kα X-ray source. The Al anode was powered at 10 mA and 15 kV. The instrument work function was calibrated to give a Au $4f_{7/2}$ metallic gold binding energy of 83.95 eV. The instrument base pressure was ca. 1×10^{-9} Torr. The analysis area size was 0.3×0.7 mm^2. For calibration purposes, the binding energies were referenced to the C 1s peak at 284.8 eV. Survey spectra were collected with a 20-eV pass energy and a step size of 1 eV. The high-resolution spectra were collected with a pass energy of 20 eV and a 0.1 eV step size. We note that we cannot rule out the effects of adventitious O and C; however, as similar analysis procedures have been consistently applied across samples, these errors become systematic, and relative trends are revealed.

12. Determination of the oxygen content of rGO and GO, and exposed Au via XPS. The atomic % of exposed oxygen, Au, or carbon on the rGO/Au composites was estimated using CasaXPS software and the sensitivity factors specific to the XPS instrument (Section 11).

13. X-Ray Diffraction Analysis. Grazing incidence X-ray diffraction (GI-XRD) measurements were performed on rGO films deposited on Au-coated aluminosilicate unless otherwise noted. The GI-XRD patterns were collected using a Rigaku SmartLab X-ray diffractometer equipped with a Cu Kα X-ray source and a HyPix-3000 detector, with a parallel slit analyzer (PSA) 0.5° in the range of 2θ=5-60°. The GI-XRD pattern (**Figure 1f**) was obtained at a 0.2° incidence angle by averaging three scans, each with a 3°/min scan rate.

14. *in-situ* ATR-IR Data Collection. The *in-situ* IR spectra on both Au and rGO on Au-coated Si prisms were sequentially acquired with a spectral resolution of 4 cm^{-1} at every 19.2(8) s interval. Prior to IR data collection, 0.1 M $HClO_4$ (pH 1.22) was added in the cell and purged for 15 min with N_2. Following purging, initial cyclic voltammetry (CV) was performed from 1.07 V vs. RHE to 0.26 V vs. RHE for 3 continuous cycles at 100 mV s^{-1} and 50 mV s^{-1}. Before recording the IR spectra, the rGO/Au or Au film was held for at least 200 sec at 1.07 V vs. RHE and a single beam spectrum (32 scans) was collected at 1.07 vs. RHE and used as the reference spectrum. All spectra were collected at a CV scan rate of 2 mV s^{-1}. All spectra were collected for the first and second CV cycle. Before the 2nd CV cycle, a new single beam spectrum was collected at 1.07 V vs. RHE and used as the reference spectrum.

15. Scanning Electron Microscopy. Scanning Electron Microscopy (SEM) imaging was performed using a Carl Zeiss Merlin Field-Emission Scanning Electron Microscope equipped with an InLens detector. The accelerating voltage was set to 3.00 kV and the beam current was set to 114 pA.

16. Electron Energy Loss Spectroscopy. Electron energy loss spectroscopy (EELS) was measured using a ThermoFisher Scientific Spectra 200 (S)TEM operated at 80kV and equipped with a Gatan Quantum SE Spectrometer. The data were acquired and processed by using DigitalMicrograph. The background was subtracted by using a power law model and the plural scattering effect was removed by using a Fourier-Ratio method. We corrected the plural scattering effect by collecting and subtracting the zero-loss spectrum for each sample. For this correction, zero loss spectra were acquired from the same area of the samples used to acquire carbon core spectra. The rGO sample was prepared by depositing rGO on Au-coated Si wafers for 8 minutes, as described in Section 4. For the rGO TEM samples, the surface of the rGO material on the Si wafer was carefully scratched using a sharp blade. Subsequently, a TEM grid was gently swept across the surface to pick up rGO material. The EELS spectrum in **Figure 1b** was smoothed over 50 points using the locally estimated scatterplot smoothing (LOESS) method in the Origin software over the entire range shown. The EELS data in **Figure S12** are on an identical rGO sample at three separate spots, and they were smoothed 21 points using the LOESS method in the Origin software over the entire range shown.

17. Computational Methods.

17.1 Preparation of rGO Models. We obtained the crystal structure of graphite from the Cambridge crystallographic database and constructed a 4×4×4 hexagonal supercell ($a = b$ =10.046 Å, c = 13.440 Å) containing 128 carbon atoms and 4 layers with an interlayer distance of 3.36 Å. From each layer, we chose a few carbon atoms and replaced them with oxygen, amounting up to 10 such replacements. Then four of such oxygens were randomly chosen and one of their nearest carbons is replaced with hydrogen atoms. This was done to consider the possibility of forming phenolic hydroxyl (-OH) groups during the following annealing simulations. Following earlier protocols,[4,5] the obtained $C_{114}O_{10}H_4$ structure is annealed at three different temperatures: 1000K, 3000K, and 5000 K, for 3 ps using first-principles molecular dynamics simulations (FPMD). For the FPMD simulations, we used Qbox code[6] and employed local density approximation (LDA) of the exchange-correlation functional[7] with a 60 Ry kinetic energy cutoff and norm-

conserving pseudopotentials.[8] FPMD sampling is performed in a canonical (NVT) ensemble where the temperature is maintained using a stochastic velocity rescaling thermostat.[9] After annealing at 3ps, we quenched it to 300 K. We allowed 0.1, 0.2, and 0.3 ps quenching time for the configurations obtained from FPMD simulations at 1000 K, 3000 K, and 5000 K, respectively. We performed another 2 ps FPMD simulations at 300 K for each of these trajectories for further equilibration.
Following the annealing-quench simulations, we continued an energy minimization of these three structures until forces on all atoms were less than 2×10^{-5} Ha/Bohr. These obtained three configurations, which are shown in ball and stick representations in **Figure S24** (a-c), are referred to as Model-1, Model-2, and Model-3, respectively. We employed a generalized gradient approximated Perdew–Burke–Ernzerhof (PBE) exchange-correlation functional[10] with a 60 Ry kinetic energy cutoff and norm-conserving pseudopotentials[8] for energy minimization and all further density functional theory (DFT) calculations. We note that Model-1 and Model-2, retained the 2-dimensional layered structure, while the Model-3, formed a 3-dimensional network of atoms. The obtained PBE band gaps for these models are 0.08, 0.01, and 0.4 eV respectively, which are consistent within the range of 0 to 1 eV provided by an earlier study on rGO-sheets with similar O/C ratios and employing the same functional.[11]

17.2 Estimation of Hybridization of Carbon Atoms. To estimate the hybridization of each carbon atom, first, we calculated the coordination number (number of covalent bonds) of each C atom. For that purpose, we calculated the maximally localized Wannier function centers (MLWFC),[12] denoted by X, using the refinement correction proposed by Stengel and Spaldin,[13] as implemented in Qbox. A carbon atom is considered to be bonded with another carbon or a hetero-atom, A, if C and A share an X within the Wannier association length (w). That is for a C—X—A triplet, C—A is considered to be bonded only if $dC{-}X{\leq}w$ and $dA{-}X{\leq}w$, where d denotes the distance. In our earlier work, we found that for amorphous carbon without heteroatoms, w=0.9 Å.[5] For a C—O bond, the MLWFC is closer to the O atom due to its high electronegativity. To include this effect, we used w=0.95 Å for these rGO samples.
The four-fold coordinated C atoms (4c-C) are sp^3 hybridized, whereas 3-fold coordinated C atoms (3c-C) may be sp^3 or sp^2 hybridized depending on the pyramidal or trigonal-planner geometry of the 3c-C atom. To distinguish between them, we computed the scaler triple product (V) of the three bond vectors, which should be zero for a perfect trigonal-planner geometry. To allow a slight fluctuation from the trigonal-planner geometry, we considered the central 3c-C atoms to be sp^2 hybridized if $V{\leq}0.25$ Å^3. Similarly, for a two-fold coordinated C atom (2c-C), we calculated the bond angle (θ) A_1—C—A_2, where A_1 and A_2 are any C or heteroatoms. We defined the central 2c-C atom to be sp, sp^2, or sp^3 hybridized depending on the following bond angle criteria: (i) $150° \leq\theta\leq 180°$, (ii) $112° \leq\theta< 150°$, and $\theta< 112°$, respectively. **Figure S24d** shows the percentage of different hybridizations of C atoms in the three different models. We note that in the 2D-layered models, we find a very high sp^2 fraction (96.5% and 97.4% for Model-1 and Model-2, respectively), whereas, for the Model-3, the sp^2 fraction reduced to 72% with an increase of sp^3 hybridized C amounting up to 23%.

17.3 Calculation of Vibrational Frequencies and IR Spectrum. The initial dynamical matrix is computed using a symmetric Cartesian displacement of amplitude 0.005 Bohr. The displacements are generated using an open-source package PyEPFD[14–16] whereas single-point DFT calculations using the PBE functional were carried out using the Qbox code. The diagonalization of the obtained dynamical matrix using PyEPFD yields the normal coordinates (Qk; k=normal mode index). Subsequently, we utilized PyEPFD to displace the atoms along each normal mode with an amplitude corresponding to a potential energy change of 0.001 Ha. We performed single-point DFT calculations on these displaced configurations and the total dipole moment (μ) was computed utilizing the positions of the MLWFCs, as implemented in Qbox.

Note, we reported the normal mode frequencies (ωk) obtained from the second derivative of the DFT total energies (E_{DFT}) with respect to the corresponding normal mode coordinates,

$$\omega_k = \sqrt{\left(\frac{\partial^2 E_{DFT}}{\partial Q_k^2}\right)_0}, \quad \text{(S1)}$$

which was shown to be numerically more accurate than that obtained from displacing the atoms in Cartesian coordinates.[17,18] Indeed, we did not find any imaginary normal-mode frequencies for none of these rGO models. The second derivative is computed using finite difference utilizing the DFT energies of the normal-mode displaced configurations.

Within the double harmonic approximation, the infrared transition probability or the oscillator strength (f_k) of each normal mode is proportional to the square of the dipole moment gradient with respect to the normal mode coordinate.[19]

$$f_k \propto \left(\frac{\partial \mu}{\partial Q_k}\right)^2 \quad \text{(S2)}$$

We computed the dipole moment gradients using finite differences, as implemented in PyEPFD, using the normal-mode displaced configurations. For a periodic system, the dipole moment is not a single vector but a lattice with several branches, and therefore, one must ensure the dipole moments of the displaced configurations entering the finite difference formula, are in the same branch.[20] For a small subset of normal modes, such a change of dipole moment branches was detected. The oscillator strengths of these modes were corrected by employing smaller normal-mode displacements (corresponding to a potential energy change of 0.0005 Ha or 0.0001 Ha).

The vibrational density of states (VDOS) and the IR spectra were broadened using a Lorentzian,

$$L_k(\omega) = \frac{\gamma}{(\omega - \omega_k)^2 + \gamma^2} \quad \text{(S3)}$$

with a broadening parameter, $\gamma = 30$ cm^{-1}. The VDOS and IR spectra of the three rGO models are shown in **Figure S25.**

17.4 Calculations in the Presence of a Finite Total Electric Field. To calculate the VDOS and IR spectra in the presence of a non-zero total electric field, DFT single-point calculations on the previously obtained normal-mode displaced configurations and the geometry-optimized configurations were repeated by changing the total electric field vector. We utilized the procedure developed by Souza et al,[21] as implemented in Qbox, where the upper limits of the total electric field are limited to the ratio of the band gap and cell lengths. This is because, at these upper limits, the onset of Zenner tunneling leads to a runaway solution of Kohn-Sham equations.[21] Owning to this intrinsic upper limit, we could not apply an electric field to Model-2 (band gap 0.01 eV), whereas for Model-1 and Model-3 (with 0.08 and 0.4 eV band gaps, respectively), we restricted the maximum total electric field to 25 and 50 MV/m, respectively. The VDOS and IR spectra were calculated as described in Section 17.3 employing equations S1-S3. Consistent with the experimentally observed layered structure perpendicular to the electrode surface (**Figure S15**), electric field effects were analyzed along the z-axis.

Supplemental Tables

Peak Position (cm^{-1})	**Assignments** [22–24]
3569	ν(C−OH, COOH, H_2O)
3374	ν(C−OH, COOH, H_2O)
3250	ν(C−OH, COOH, H_2O)
2812	C−H
1734	ν(C=O)
1621	ν(C=O) + ν(C−OH)
1579 (shoulder)	ν(C=C)
1344	ν_{asym}(C−O−C) + ν(C=O)
1265 (shoulder)	ν_{asym}(C−O−C)
1226	ν_{asym}(C−O−C)
1054	ν(C−OH) phenol

Table S1. IR peak assignments of bulk GO in the absence of applied potential. Corresponding IR spectrum in **Figure S7**, black. Peak assignments are based off literature precedent as referenced. We note that the literature utilizes computed molecular models to assign GO features.

Assignments[22–27]	**Peak Position (cm^{-1})**
rGO ν(C=O) + ν(COOH)	1707
complex C=C modes (this work)	1553
Si phonon	1490
Si phonon	1401
Si phonon	1205

Table S2. IR peak assignments of bulk rGO in the absence of applied potential. Corresponding IR spectrum in **Figure S8**, black. Peak assignments are based off literature precedent as referenced. We note that the literature utilizes computed molecular models to assign IR features of carbon. We also note that rGO features that may be present at wavenumbers lower than 1500 cm^{-1} can be dominated by well-documented Si phonon modes.[25–27]

Measurement	**GO**	**rGO**
O/C Ratio	0.39 (27.6/70.7)	0.14 (11.9/83.8)

Table S3. O/C ratio of GO and rGO. GO was dropcast onto Au-coated Si wafer and rGO was a representative thin film on Au-coated Si prism. Ratio was calculated from the O and C peaks in their survey XPS spectra, **Figures S10** and **S11**.

Element	GO (at %)	rGO (at %)
C	70.7	83.8
O	27.6	11.9
Au	1.1	0.1
Si	-	0.9
Na	0.6	2.7
S	-	0.6

Table S4. Atomic percentages of all elements observed in GO and rGO. GO was dropcast onto a Au-coated Si wafer and rGO was a representative thin film on a Au-coated Si prism. Elemental analysis was performed using survey XPS spectra, **Figures S10** and **S11**.

Position at 0.89 V vs RHE (cm^{-1})	Position at 0.29 V vs RHE (cm^{-1})	Position at 0.87 V vs RHE (cm^{-1})	Assignment
1269	1264	1270	rGO (this work)
1585	1592	1589	rGO (this work)
--	1650	1644	δ(HOH)[28]

Table S5. IR peak positions and assignments of rGO on Au-coated Si in N_2-saturated 0.1 M $HClO_4$. IR spectra are shown in **Figure 2b**. Data at 0.89 V report on wavenumber values on the forward-going CV trace, and data at 0.87 V report on wavenumber values on the reverse-going CV trace.

Position at 0.89 V vs RHE (cm^{-1})	Position at 0.29 V vs RHE (cm^{-1})	Position at 0.87 V vs RHE (cm^{-1})	Assignment
1191	1190	1190	δ(DOD)[29]
1274	1271	1275	rGO (this work)
1581	1589	1584	rGO (this work)

Table S6. IR peak positions and assignments of rGO on Au-coated Si in N_2-saturated 0.1 M DCl in D_2O. IR spectra shown in **Figure S19**. Data at 0.89 V report on wavenumber values on the forward-going CV trace, and data at 0.87 V report on wavenumber values on the reverse-going CV trace.

Position at 0.89 V vs RHE (cm^{-1})	Position at 0.29 V vs RHE (cm^{-1})	Position at 0.87 V vs RHE (cm^{-1})	Assignment
1644	1656	1640	δ(HOH)[28]

Table S7. IR peak positions and assignments of Au in N_2 saturated 0.1 M $HClO_4$. IR spectra shown in **Figure S21**. Data at 0.89 V report on wavenumber values on the forward-going CV trace, and data at 0.87 V report on wavenumber values on the reverse-going CV trace.

Position at 0.89 V vs RHE (cm^{-1})	Position at 0.29 V vs RHE (cm^{-1})	Position at 0.87 V vs RHE (cm^{-1}) (cm^{-1})	Assignment
1275	1267	1274	rGO
1581	1588	1586	rGO
---	1666	1642	δ(HOH)[28]

Table S8. IR peak positions and assignments of 0.3 μm thick rGO on Au-coated Si in N_2 saturated 0.1 M $HClO_4$. IR spectra shown in **Figure S22**. Data at 0.89 V report on wavenumber values on the forward-going CV trace, and data at 0.87 V report on wavenumber values on the reverse-going CV trace.

Mode Number	Peak Position (cm^{-1})	Figure Depicted the IR spectrum and Contributing Vibrational Modes
I	1598	S25b, brown + S26 (i)
II	1518	S25b, brown + S26 (h)
III	1407	S25b, brown + S26 (g)
IV	1390	S25b, brown + S26 (f)
V	1224	S25b, brown + S26 (b-e)
VI	1182	S25b, brown + S26 (a)

Table S9. Calculated IR peaks of Model-1, $C_{114}O_{10}H_4$ in the absence of an applied electric field (at 0 MV m^{-1}).

Supplemental Figures

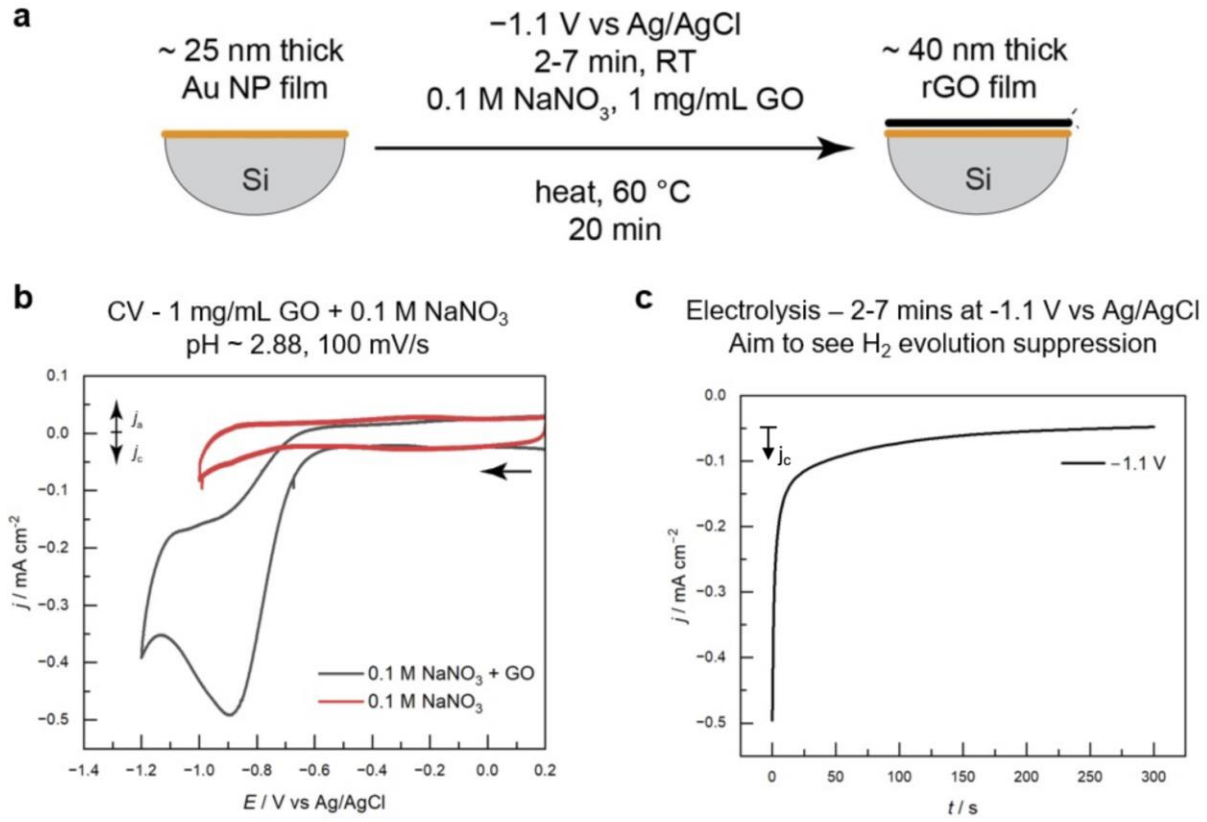

Figure S1. Representative electrodeposition of rGO onto a Au film. **(a)** Schematic of electrodeposition conditions. (**b**) Cyclic voltammogram of an Au disk electrode taken in the presence of 0.1 M $NaNO_3$ (red trace) compared to 0.1 M $NaNO_3$ and 1 mg/mL GO (black trace) recorded at 100 mV s^{-1}. The reductive feature observed at –0.88 V vs Ag/AgCl is within the range of reported deposition potentials attributed to the electrochemical reduction of the oxidic functionalities on GO.[3,30] The reductive feature is also observed when 0.1 M $NaNO_3$ is acidified to pH 2.7 in the absence of exogenously added GO (**Figure S2**). These results suggest that the reductive features observed at –0.88 V vs Ag/AgCl in the presence of GO (**Figure S1b**) can be attributed to both the reduction of GO as well as HNO_3 in the bulk electrolyte as it is acidified upon GO addition (GO pK_a ~ 4.3, 6.6, 9.8)[31–33]. **(c)** Chronoamperometry trace of an Au disk electrode taken in the presence of 1 mg/mL GO and 0.1 M $NaNO_3$ at –1.1 V vs Ag/AgCl. The chronoamperometry results in the formation of a black film on the Au surface. We obtained a featureless voltametric profile of this black film in 0.1 M sodium phosphate (pH 7.4) over a wide potential range under N_2 conditions. This result is in line with the voltametric profile observed using a glassy carbon electrode (**Figure S3**) and inconsistent with that observed on a pristine Au surface where the surface catalyzes the hydrogen evolution reaction (HER) (**Figure S3**), suggesting a complete suppression of the HER by the carbon film over the potential range examined.

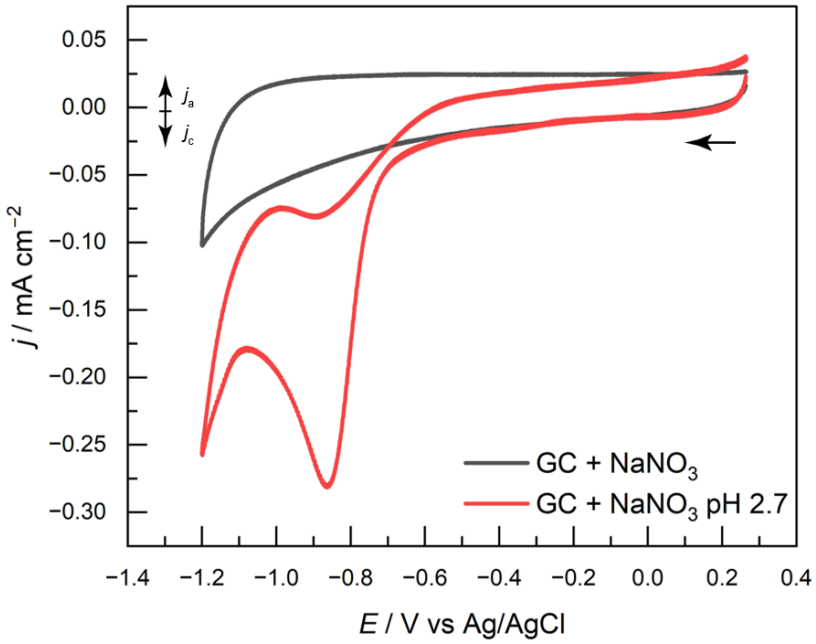

Figure S2. Cyclic voltammogram of a glassy carbon disk electrode in the presence of 0.1 M $NaNO_3$ (black) and in the presence of 0.1 M $NaNO_3$ acidified to pH 2.7 using HNO_3. Data are collected at 100 mV s^{-1} with a negative direction of scan.

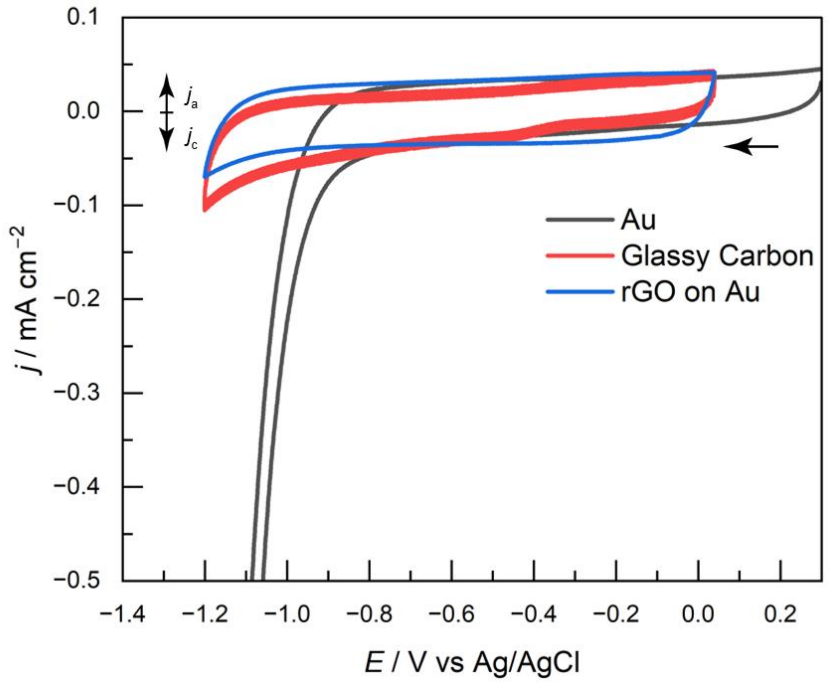

Figure S3. Cyclic voltammogram of an Au foil electrode (black), glassy carbon foil electrode (red), and rGO deposited on a Au foil electrode (blue) in 0.1 M sodium phosphate buffer, pH 7.4. Data are collected at 100 mV s^{-1} with a negative direction of scan. We note that the current density of the data reported for the rGO/Au foil (blue) is scaled by a factor of 0.01 to facilitate comparison of the cathodic current within the same potential range.

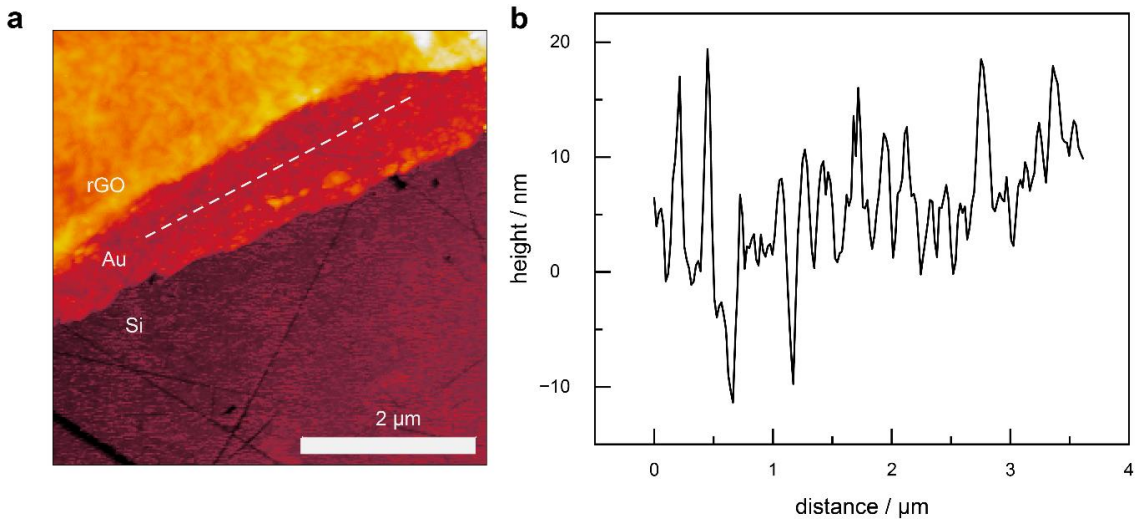

Figure S4. Atomic force microscopy (AFM) characterization of the morphology of the underlying Au film in rGO/Si/Au. (**a**) AFM image of the rGO/Si/Au boundary. The white dotted line indicates the section analyzed in **b**. (**b**) The height profile along the white dotted line in panel **a**, showing the nanostructure of the underlying Au film. The particle diameter was calculated as the average distance between the peaks in the height profile (210 nm), consistent with an island-like morphology of the underlying Au film.

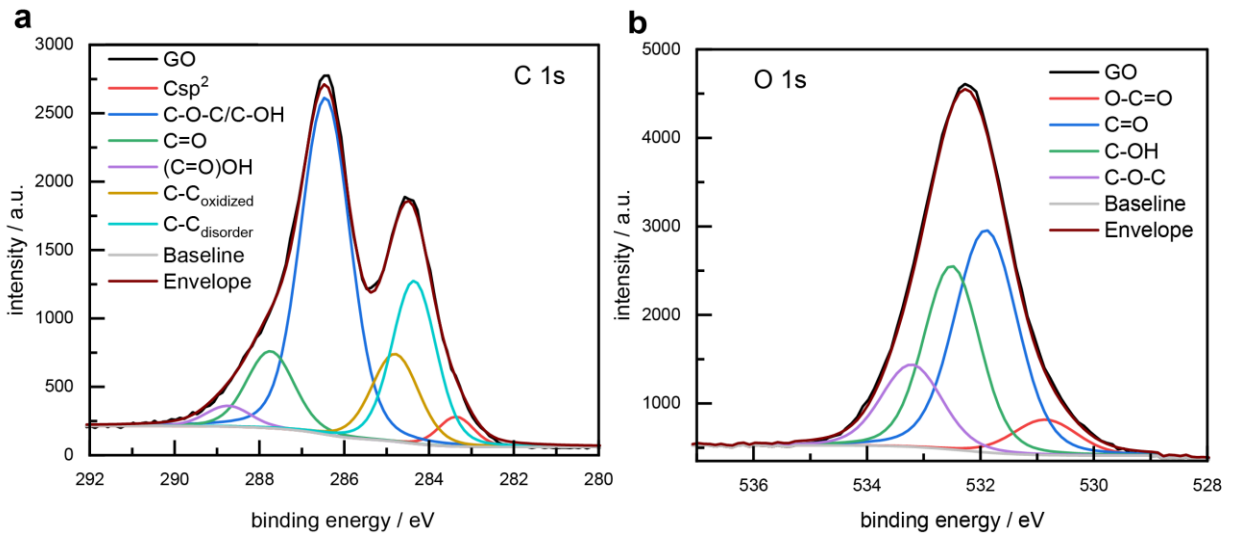

Figure S5. Deconvoluted high-resolution x-ray photoelectron spectra of the (**a**) C 1s and the (**b**) O 1s region of GO dropcast onto Au-coated Si wafer. In (**a**), red corresponds to graphite-like C sp^2 at 283.4 eV; blue corresponds to ether and hydroxyl (C–O–C/C–OH) at 286.4 eV; green corresponds to carbonyl (C=O) at 287.7 eV; purple corresponds to carboxylic acid ((C=O)OH) at 288.7 eV; yellow corresponds to carbons bound to oxidized carbons ($C–C_{oxidized}$) at 284.8 eV; aqua corresponds to carbons in disordered regions, i.e. near sp^3 carbons, vacancies, edges, pentagons, and heptagons ($C–C_{disorder}$) at 284.4 eV. In (**b**), red corresponds to carboxylic acid and ester (O–C=O) at 530.9 eV; blue corresponds to carbonyl (C=O) at 531.9 eV; green corresponds to hydroxyl (C–OH) at 532.5 eV; purple corresponds to ether (C–O–C) at 533.2 eV. Chemical environments were assigned by comparing the peak positions observed in our XPS spectra with that of previous reports.[34–36]

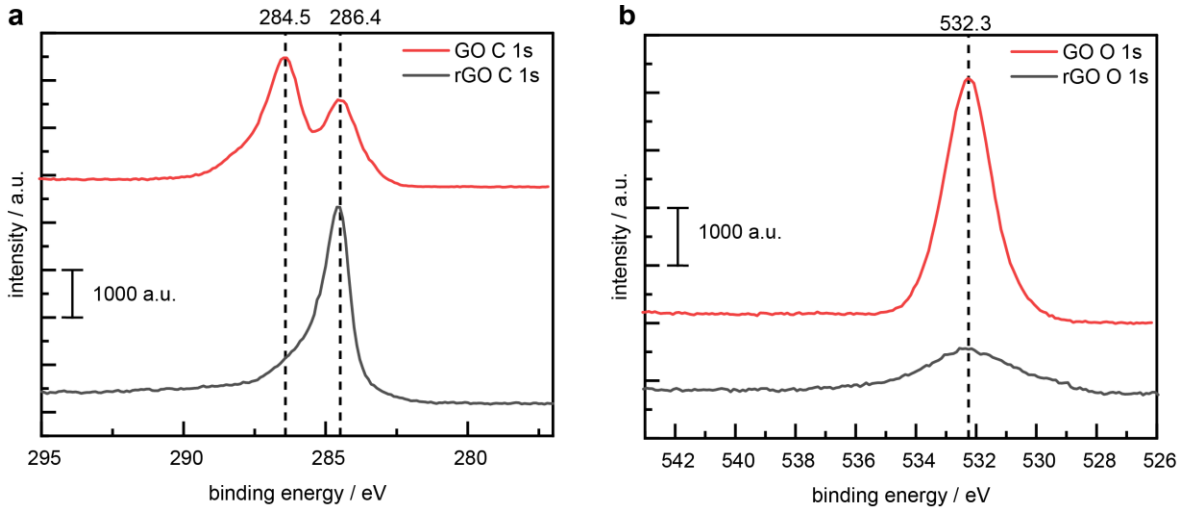

Figure S6. Comparison of high-resolution XPS spectra of rGO (black) and GO (red) of (**a**) C 1s and (**b**) O 1s regions.

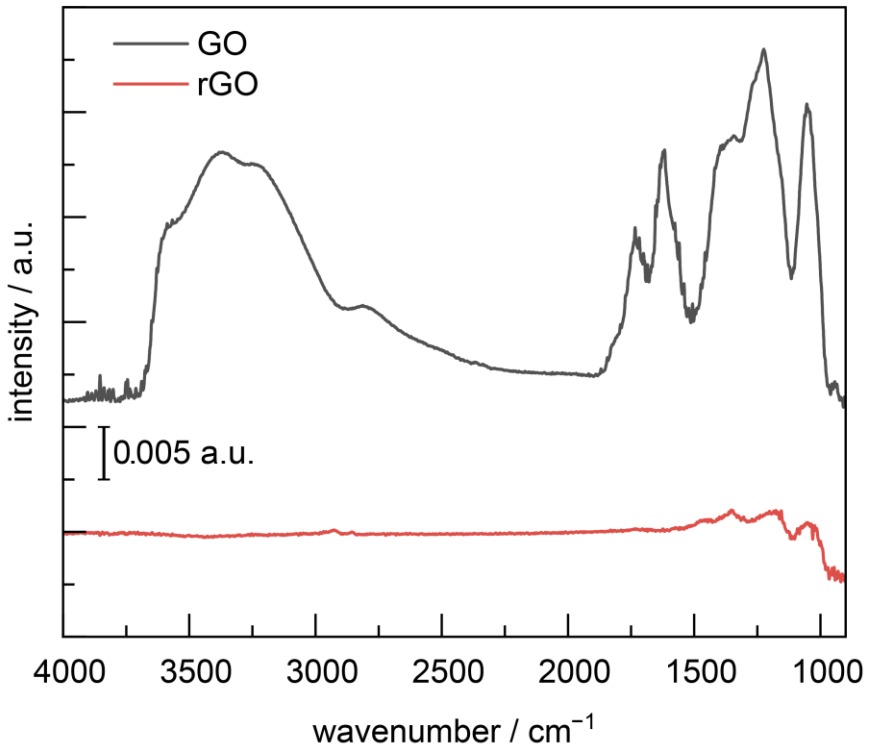

Figure S7. ATR-IR spectra of bulk GO and rGO collected in the absence of applied potential on a Si prism. The background spectrum for both traces is the bare Si prism. For peak assignments see **Tables S1** and **S2**.

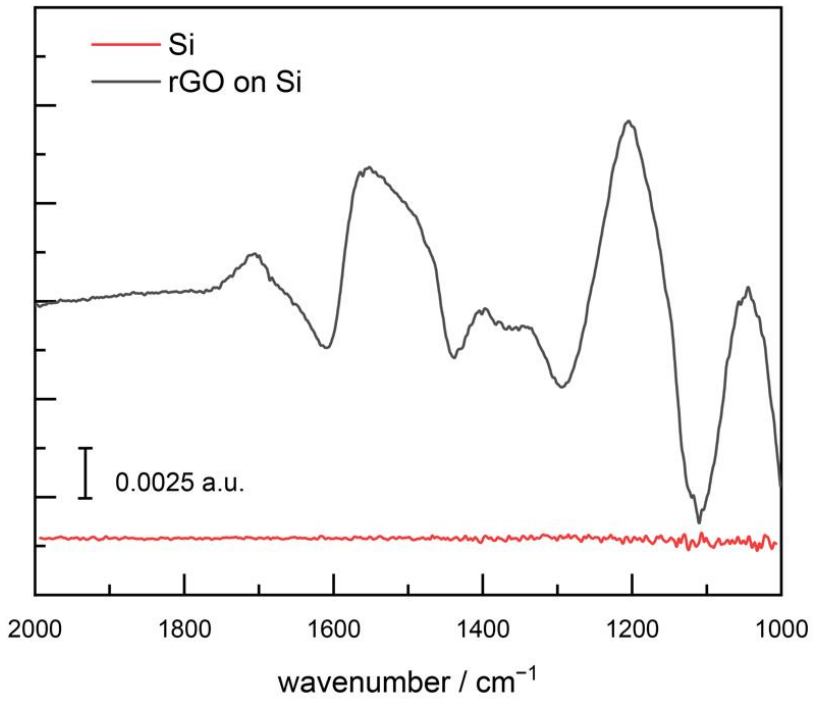

Figure S8. ATR-IR spectrum of rGO, **black**, collected on an undoped Si prism in the absence of applied potential. The rGO trace shown is a magnified view of the same data shown in **Figure S7**, red. The background spectrum is the bare Si prism. A spectrum collected using the bare Si prism without rGO is shown in red. For peak assignments see **Table S2**.

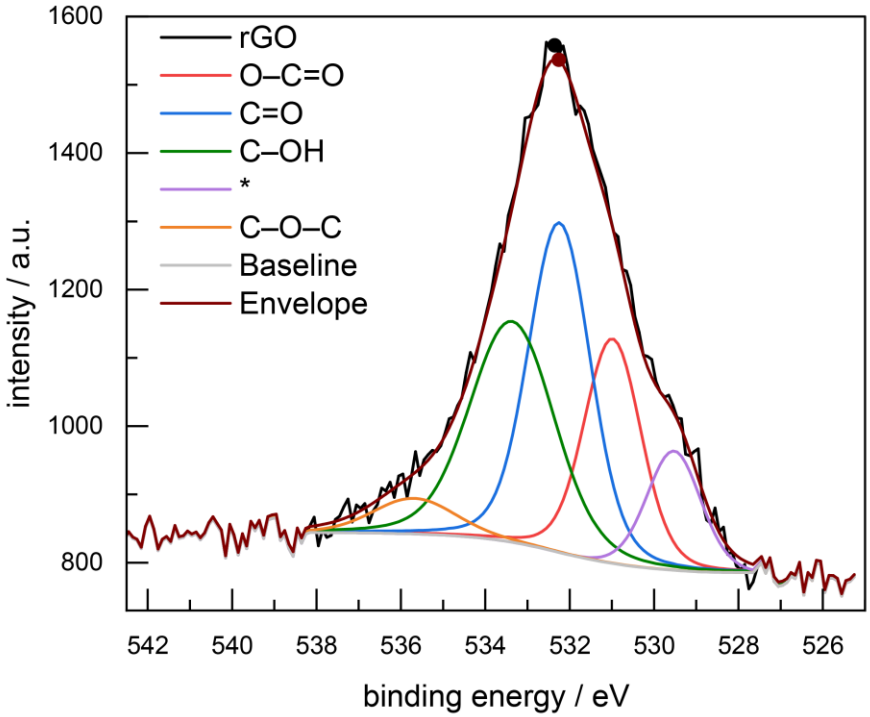

Figure S9. Deconvoluted O 1s high-resolution x-ray photoelectron spectrum of rGO on Au-coated Si prism.[37–39] We note that the O 1 s peak of the rGO film on an Au surface is broader than that of GO dropcast on Au (**Figure S5b**). To account for this broadness, we fit a new peak, purple (*), at 529.5 eV that makes up a small fraction of the overall rGO O 1s spectrum. This peak cannot be assigned with an analogous motif in the GO O 1s spectrum, and it cannot be correlated with a distinct feature in the rGO C 1s XPS. Thus, we hypothesize that this broadness can be attributed to charging effects or a distinct oxygen environment such as oxides on the substrate itself. Red corresponds to carboxylic acid and ester (O–C=O) at 531 eV; blue corresponds to carbonyl (C=O) at 532.2 eV; green corresponds to hydroxyl (C–OH) at 533.4 eV; purple corresponds to charging effects or a distinct oxygen environment such as oxides on the substrate itself (*), see above; orange corresponds to ether (C–O–C) at 535.7 eV. Chemical environments were assigned by comparing the peak positions observed in our XPS spectra with that of previous reports.[34–36]

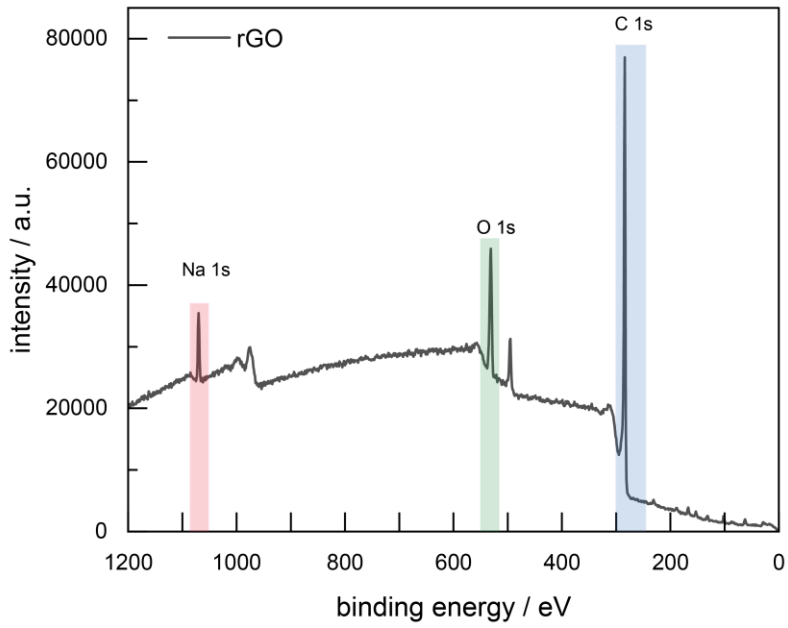

Figure S10. Survey x-ray photoelectron spectrum after rGO electrodeposition on a Au-coated Si prism. The highlighted regions represent the C 1s (blue), O 1s (green), and Na 1s (red) peaks.

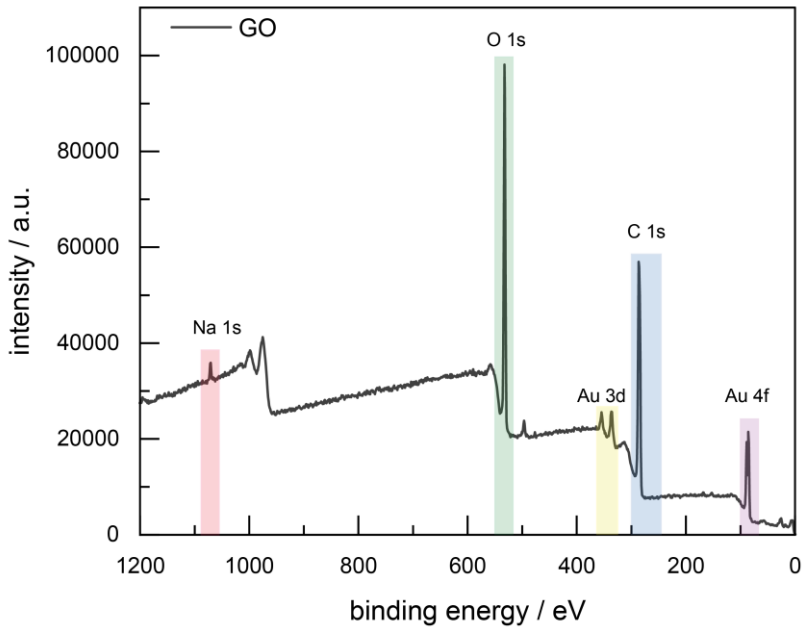

Figure S11. Survey x-ray photoelectron spectrum after GO drop cast on a Au-coated Si wafer. Au pinholes are present in this spectrum, but this is expected because of the dropcast procedure used. The main objective is to observe a change in the relative oxygen and carbon content. The highlighted regions represent the C 1s (blue), O 1s (green), Na 1s (red) peaks, Au 3d (yellow), and Au 4f (purple) peaks.

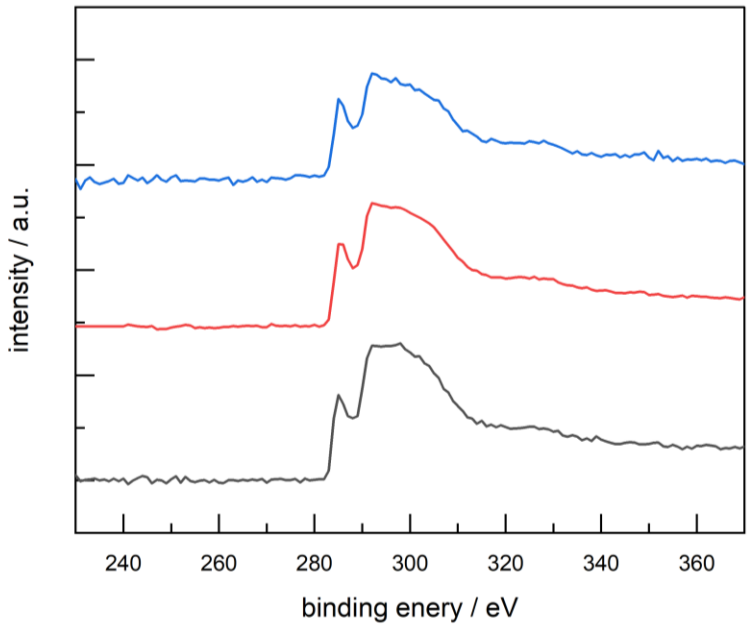

Figure S12. Various electron energy-loss spectra (EELS) of carbon K-edges on an identical rGO sample at three separate spots, indicated by blue, red, and black.

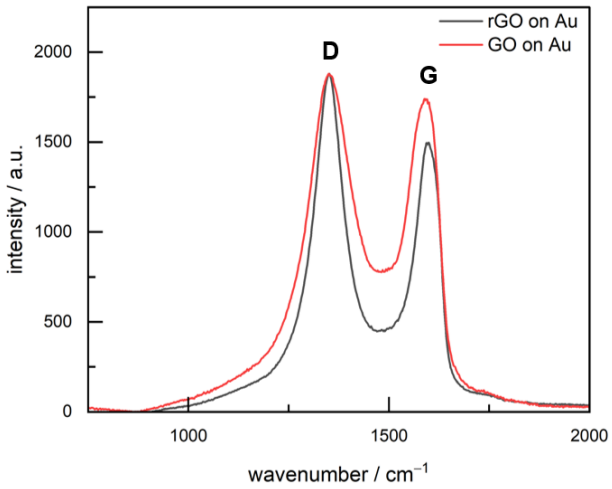

Figure S13. Raman spectra of rGO and GO. Raman spectra of rGO (black) and GO (red) on a Au-coated Si wafer showing the D and G modes.

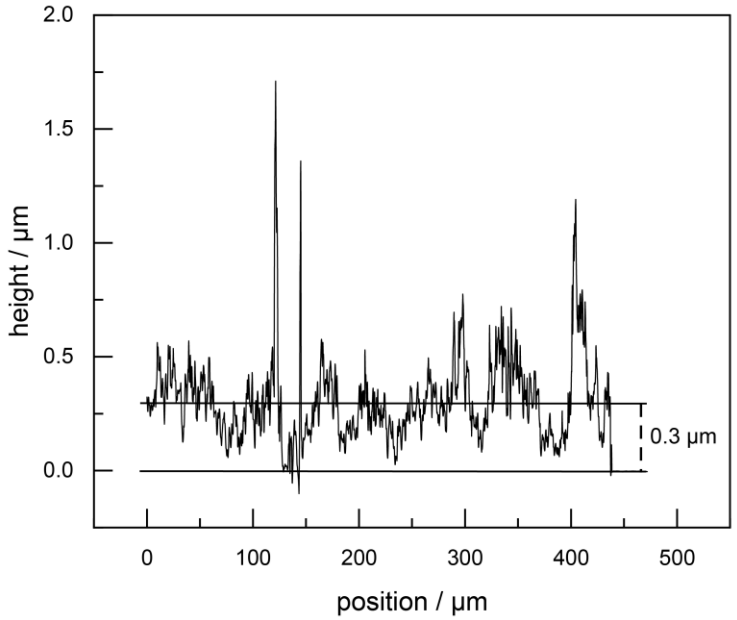

Figure S14. Profilometry profile of thick rGO on a Au-coated aluminosilicate glass slide. The horizontal black line at 0 µm corresponds to the Au layer. The horizontal line at 0.3 µm corresponds to the average height of the rGO film, which is 0.3 µm.

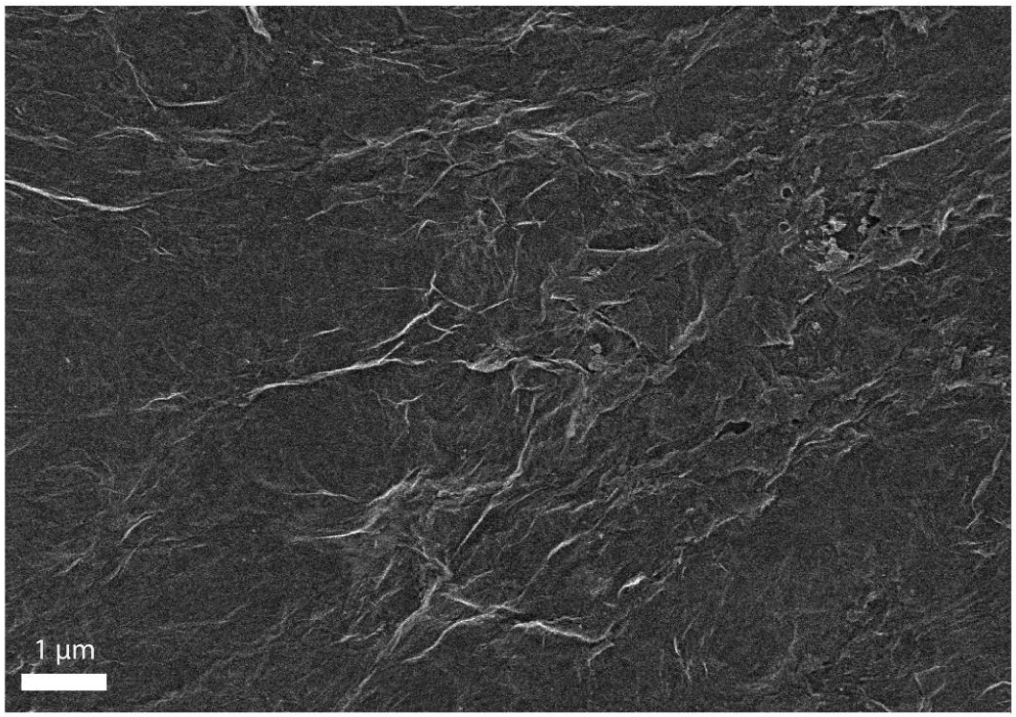

Figure S15. SEM image of 0.3-µm thick rGO on a polycrystalline Au-coated aluminosilicate slide from the top. Image obtained at a magnification of 9.71 K X.

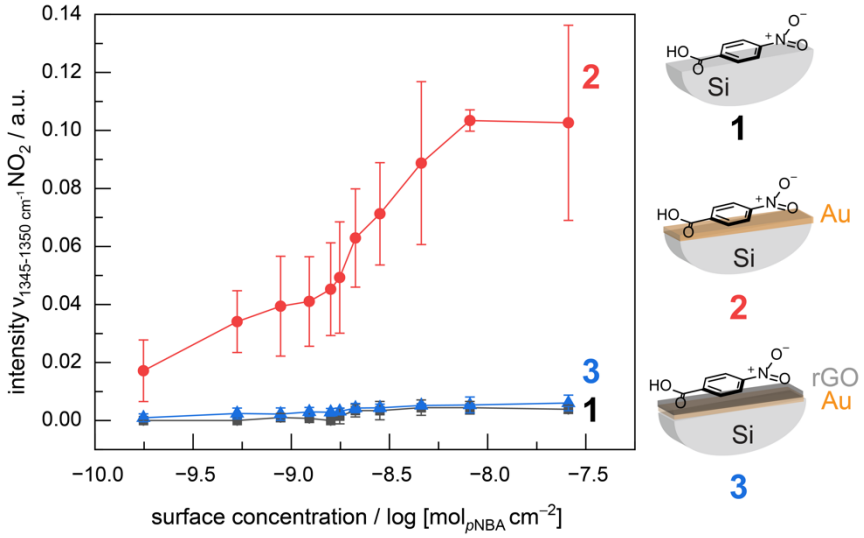

Figure S16. Comparison of the integrated band intensity of the IR peak assigned to ν_{sym}, NO_2 (1345-1350 cm^{-1}) for ATR-IR spectra collected as a function of the surface concentration of *p*-nitrobenzoic acid dropcast on (**1**, black) the surface of Si prism (**2**, red) the surface of Au-coated Si, and (**3**, blue) the surface of rGO prepared on Au-coated Si. Data points and error bars represent the average and standard deviation of three runs on independently prepared films, respectively. **1**-**3** depict simplified schematics for the deposition of *para*-nitrobenzoic acid; the molecule is not drawn to scale and neighboring molecules are omitted for clarity.

To demonstrate that the rGO prepared on Au/Si are compatible with ATR-IR characterization of the bulk carbon material, we use a probe substrate, *p*-nitrobenzoic acid, to assess if the IR beam penetrates the rGO/Au/Si composite in an ATR configuration and to assess the influence of the underlying Au nanostructure in affecting IR spectroscopic signals. First, to assess if the IR beam penetrates the rGO/Au/Si composite, we compared the IR signal intensity of *p*-nitrobenzoic acid that was deposited onto the film to that dropcast on bare Si. We systematically dropcast increasing amounts of *p*-nitrobenzoic acid onto a defined geometric surface area of the rGO/Au/Si film to track the IR absorption intensity of the well-characterized symmetric NO_2 stretch ($\nu_{sym,\ NO2}$)[40,41] as a function of the *p*-nitrobenzoic acid surface concentration and compared this result (**3** in **Figure S16**) to the same experiments performed on bare Si (**1** in **Figure S16**) under identical optical ATR configurations (see Section 10 for details). As the surface concentration of *p*-nitrobenzoic acid increases to 8.12 nmol cm^{-2}, we resolve a distinct feature at 1350 cm^{-1} for both surfaces, consistent with prior assignments of $\nu_{sym,\ NO2}$.[40,41] (**Figure S17b**). These results indicate that, although the rGO/Au layer can reduce the IR penetration depth in the ATR configuration, if the rGO/Au layer attenuates the IR penetration depth to less than the composite's thickness, vibrational probes on the surface would not produce detectable IR signals that mirror that observed on bare Si. Second, to assess the influence of the underlying Au nanostructure on IR spectroscopic signals, we performed the same titration experiment of *p*-nitrobenzoic acid addition to Si/Au. Nanostructured Au surfaces are well-known to enhance the IR absorption of species within ~8 nm of the surface; the consensus mechanism of surface-enhanced infrared absorption (SEIRA) using nanoscale metal particles, such as Au, involves their polarization induced by the incident IR light to generate an enhanced local electric field.[42–44] Thus, nanostructured Au surfaces amplify the local electric field of nearby adsorbates, thereby enhancing molecular vibrations.[45,46] On Au/Si, at a surface concentration of *p*-nitrobenzoic acid as low as 0.18 nmol cm^{-2}, we observe a distinct feature at 1345 cm^{-1} (**Figure S17a**), consistent with prior assignments of $\nu_{sym,\ NO2}$.[40,41] In contrast, on bare Si as well as on rGO/Au/Si, we observe negligible IR absorption at 1345 cm^{-1} at this low surface concentration value (**Figure S17a**). Indeed, even at a higher concentration value of 8.12 nmol cm^{-2}, the integrated band intensity for the peak assigned to $\nu_{sym,\ NO2}$ is roughly 100-fold greater

on Au/Si (**Figure S16**, **2**) than on bare Si (**Figure S16**, **1**) or rGO/Au/Si (**Figure S16**, **3**). This observed enhancement of the $\nu_{sym,\ NO2}$ IR absorption on Au/Si surfaces is consistent with the well-documented SEIRA effect for nanostructured Au.[42–46] Importantly, the similarity in the $\nu_{sym,\ NO2}$ IR signal intensity for *para*-nitrobenzoic acid systematically deposited on rGO prepared on Au/Si with bare Si (**Figure S16**, blue and black) suggests that the presence of the nanostructured Au surface underneath rGO does not serve to enhance the IR spectroscopic signals of the carbon material. Together, these results demonstrate that rGO prepared on Au/Si are compatible with ATR-IR characterization of the bulk carbon material.

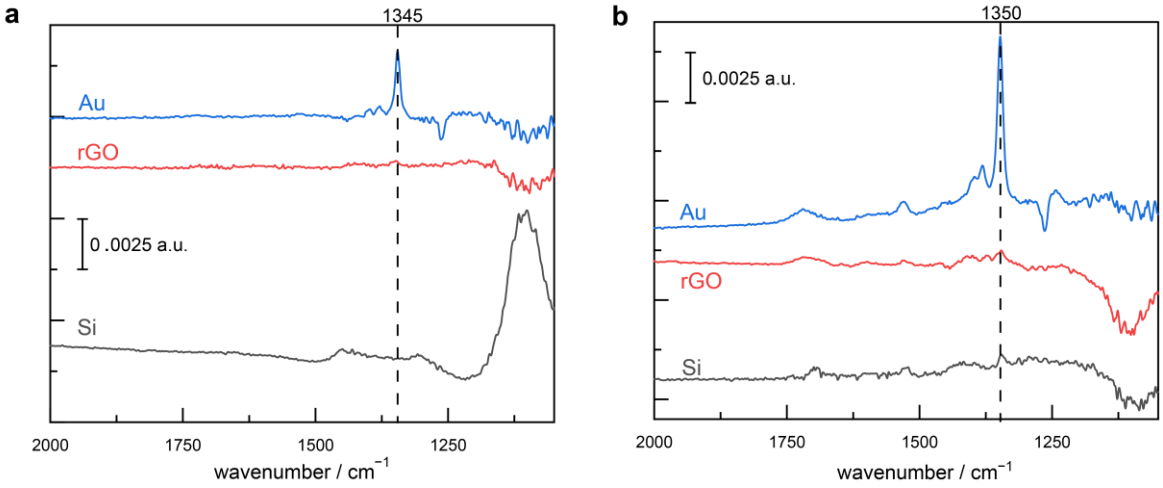

Figure S17. SEIRA spectra of *p*-nitrobenzoic acid dropcast onto Au (blue) and ATR-IR spectra of *p*-nitrobenzoic acid drop-cast onto rGO (red) and Si (black) surfaces at a surface concentration of (**a**) 0.180 nm cm^{-2} and (**b**) 8.12 nm cm^{-2}. The background for Au, rGO, and Si is bare Au, rGO, and Si, respectively, prior to any *p*-nitrobenzoic acid addition.

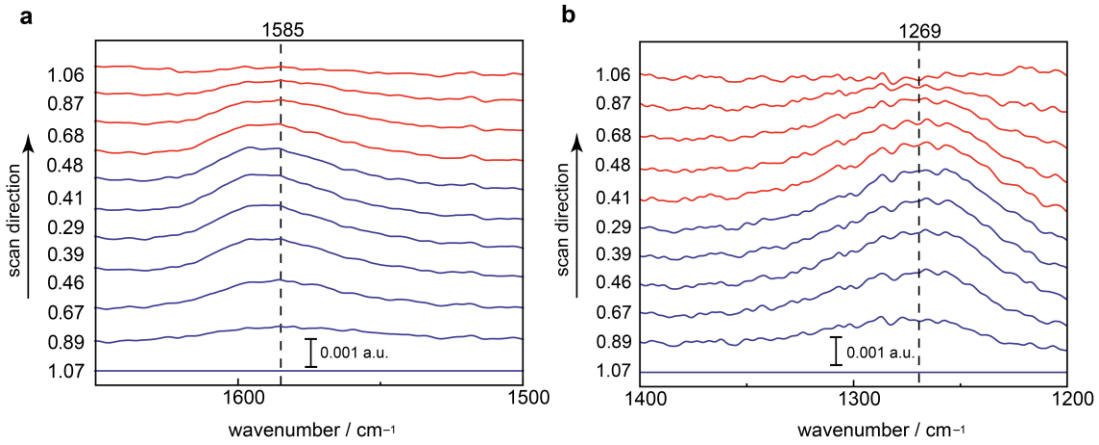

Figure S18. Magnified view of the IR spectra in **Figure 2b** of rGO on Au/Si in N_2-saturated 0.1 M $HClO_4$ taken during the CV in **Figure 2a**. Background spectra were collected in N_2-saturated 0.1 M $HClO_4$ at 1.07 V vs RHE. (**a**) ATR-IR spectra in the region 1640-1500 cm^{-1}. (**b**) ATR-IR spectra in the region from 1400-1200 cm^{-1}. Potential dependence is plotted in **Figure 2c**.

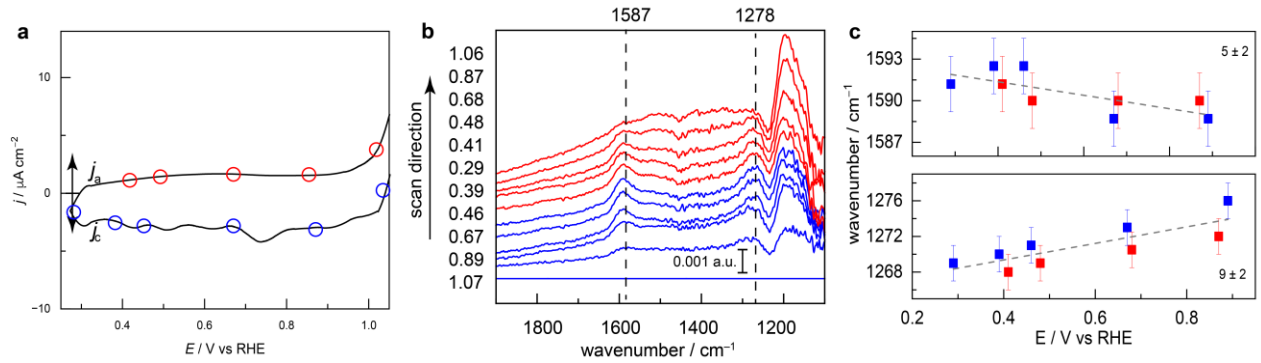

Figure S19. Cyclic voltammogram, simultaneous IR, and potential dependence of IR peak position of rGO on Au in N_2-saturated 0.1 M DCl in D_2O. (**a**) CV of rGO on Au in 0.1 M DCl in D_2O under N_2-saturated conditions. Data collected at 2 mV s^{-1} with a negative direction of scan. Blue circles represent potentials where ATR-IR spectra are reported in the negative-going scan and red circles represent potentials where ATR-IR spectra are reported in the positive-going scan in b. (**b**) Simultaneously collected ATR-IR spectra during the CV scan shown in **Figure S19a**. Background spectra were collected in N_2-saturated 0.1 M DCl at 1.07 V vs RHE. **(c)** (top) Potential dependence of the peak position of that observed at 1585 cm^{-1} at 0.89 V in **Figure S19b**. (bottom) Potential dependence of the peak position of that observed at 1269 cm^{-1} at 0.89 V in **Figure S19b**. We note that the dynamics of the 1269 cm^{-1} feature are convoluted due to presence of the D_2O bending mode at 1190 cm^{-1}, however, the trends of the shifts observed in **Figure 2** remain. Error bars depict the spectral resolution.

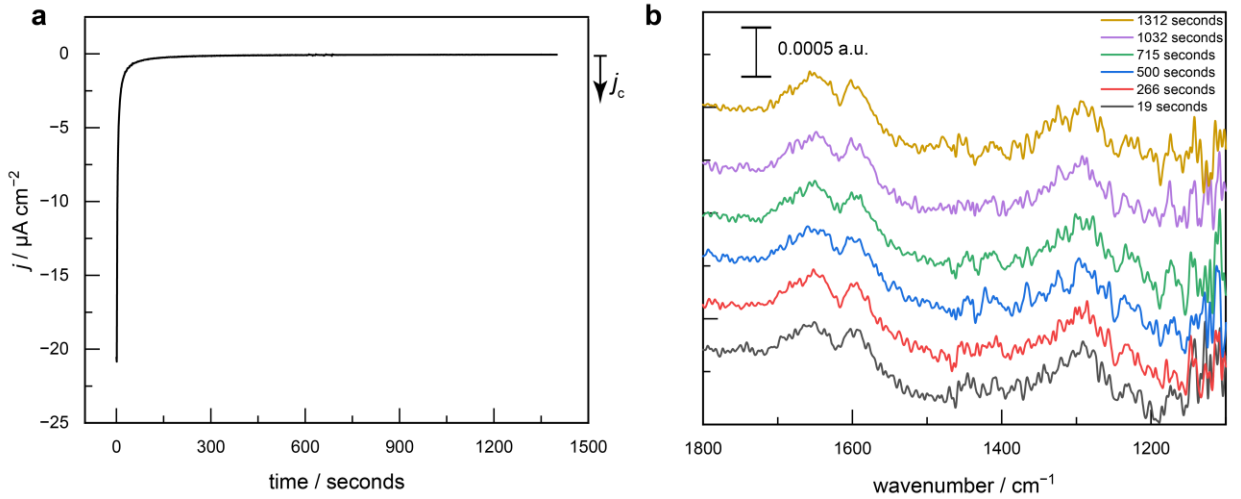

Figure S20. Chronoamperometry and simultaneous IR spectra of rGO on Au in N_2-saturated 0.1 M $HClO_4$. (**a**) Chronoamperometry trace of rGO on Au-coated Si prism in 0.1 M $HClO_4$ under N_2 saturated conditions at 0.47 V vs RHE. **(b)** Relative ATR-IR spectra of rGO on Au-coated Si prism in 0.1 M $HClO_4$ under N_2 saturated conditions collected simultaneously to the chronoamperometry at 0.47 V vs RHE. The background spectrum was collected after holding the potential at 1.07 V vs RHE for 200 seconds.

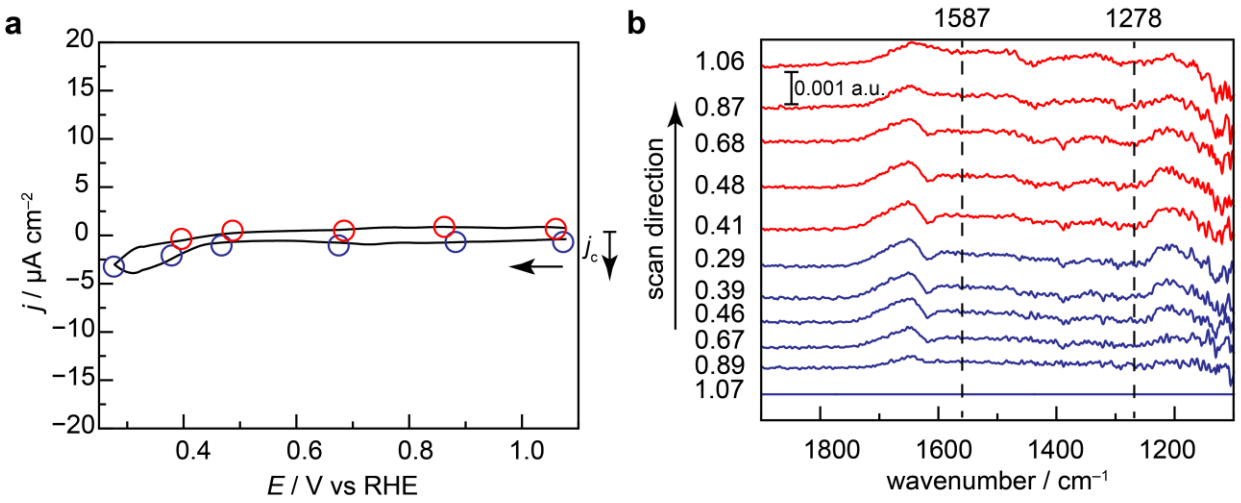

Figure S21. Cyclic voltammogram and simultaneous IR of Au films in N_2-saturated 0.1 M $HClO_4$. (**a**) CV of Au-coated Si prism in 0.1 M $HClO_4$ under N_2 saturated conditions. Data collected at 2 mV s^{-1} with a negative direction of scan. Blue circles represent potentials where SEIRA spectra are reported in the negative-going scan and red circles represent potentials where SEIRA spectra are reported in the positive-going scan in **b**. (**b**) Simultaneously collected SEIRA spectra during the CV scan shown in **a**. Background spectra were collected in N_2-saturated 0.1 M $HClO_4$ at 1.07 V vs RHE.

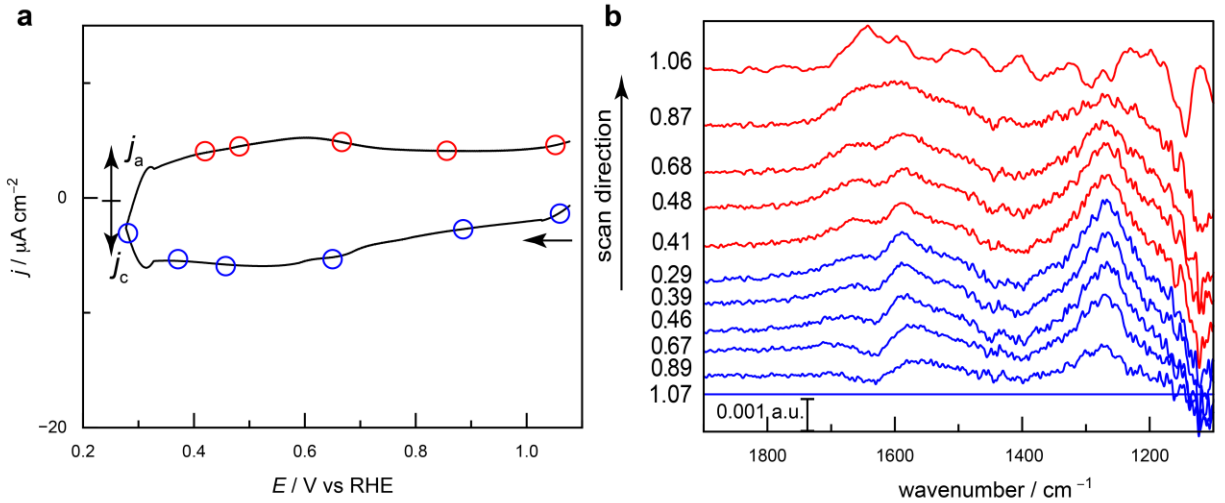

Figure S22. Cyclic voltammogram and simultaneous IR spectra of 0.3 μm thick rGO on Au in N_2-saturated 0.1 M $HClO_4$. **(a)** CV of ~ 0.3-μm thick rGO on Au-coated Si prism in 0.1 M $HClO_4$ under N_2-saturated conditions. Data collected at 2 mV s^{-1} with a negative direction of scan. Blue circles represent potentials where ATR-IR spectra are reported in the negative-going scan and red circles represent potentials where ATR-IR spectra are reported in the positive-going scan in **b**. (**b**) Simultaneously collected ATR-IR spectra during the CV scan shown in **a**. Background spectra were collected in N_2 saturated 0.1 M $HClO_4$ at 1.07 V vs RHE.

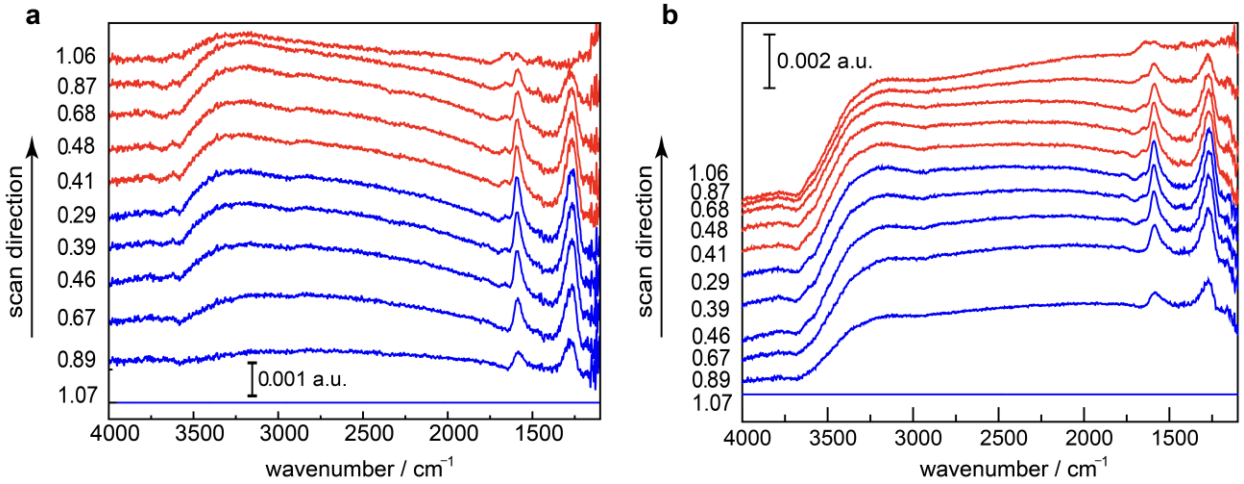

Figure S23. Full range of IR spectra taken during the CV conditions in **Figure 2**. ATR-IR spectra collected during the CV conditions presented in **Figure 2a** in the main text. The range has been expanded to include the full IR wavenumber range (1100 to 4000 cm^{-1}). **(a)** Full IR range of the spectra recorded during the first CV cycle **(b)** Full IR range of spectra recorded during the second CV cycle**.** Spectra collected during the negative direction of scan (blue) and positive direction of scan (red). We note that the baseline shifts at approximately 3000 cm^{-1}. We observe similar shifts in the absence of rGO, suggesting that the variation can reflect changes in the reflectance and absorbance of the underlying Au layer.[47–50]

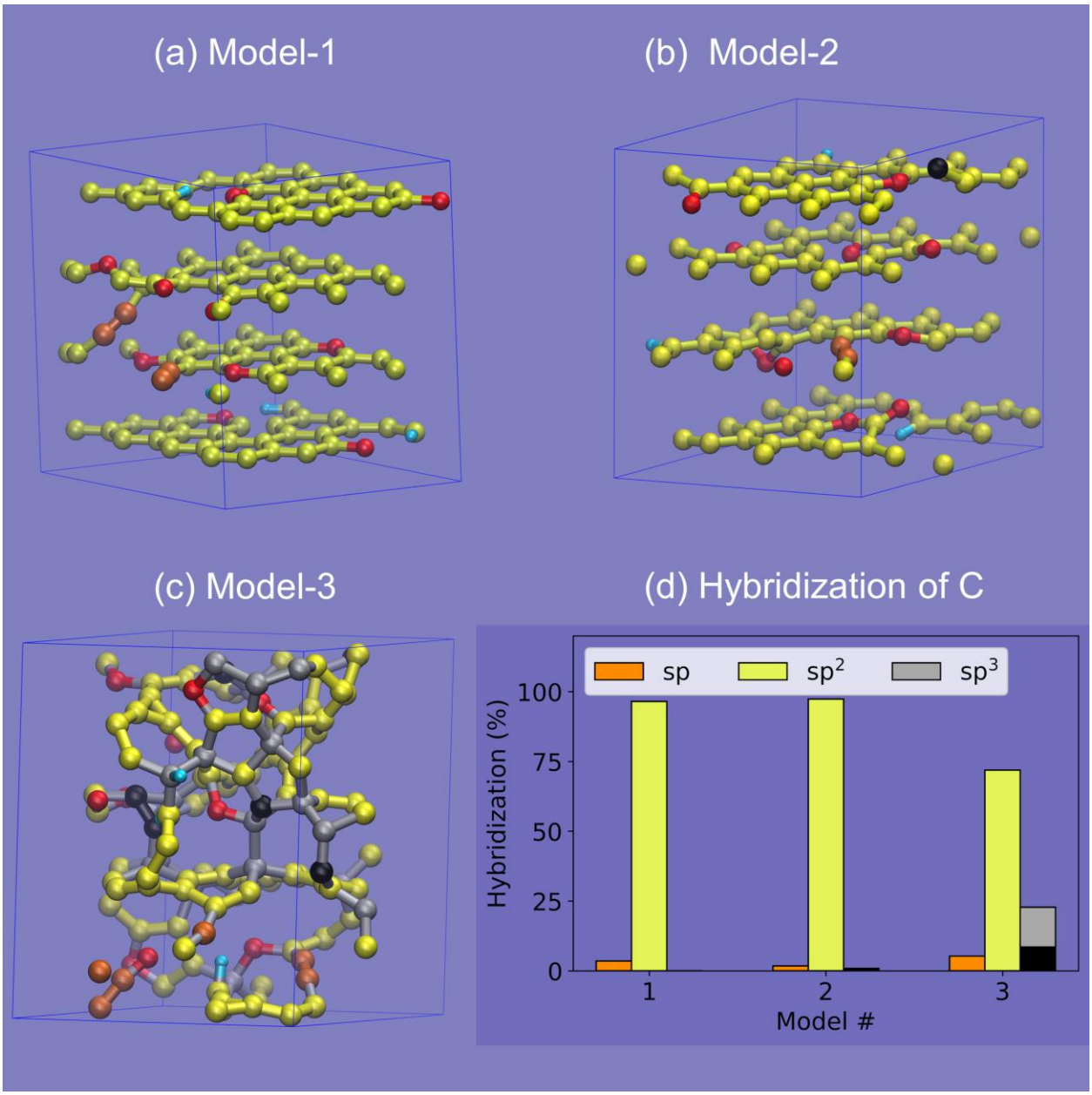

Figure S24. Ball and stick representation of three rGO models and their percentage of differently hybridized carbon. **(a-c)** Ball and stick representation of three rGO models ($C_{114}O_{10}H_4$). Red and cyan spheres represent oxygen and hydrogen atoms. Grey spheres represent saturated (4-coordinated) sp^3 hybridized carbons, whereas black spheres represent unsaturated sp^3 hybridized carbons. Yellow and orange spheres represent sp^2 and sp hybridized carbons, respectively. **(d)** The percentage of differently hybridized carbons as a function of model number.

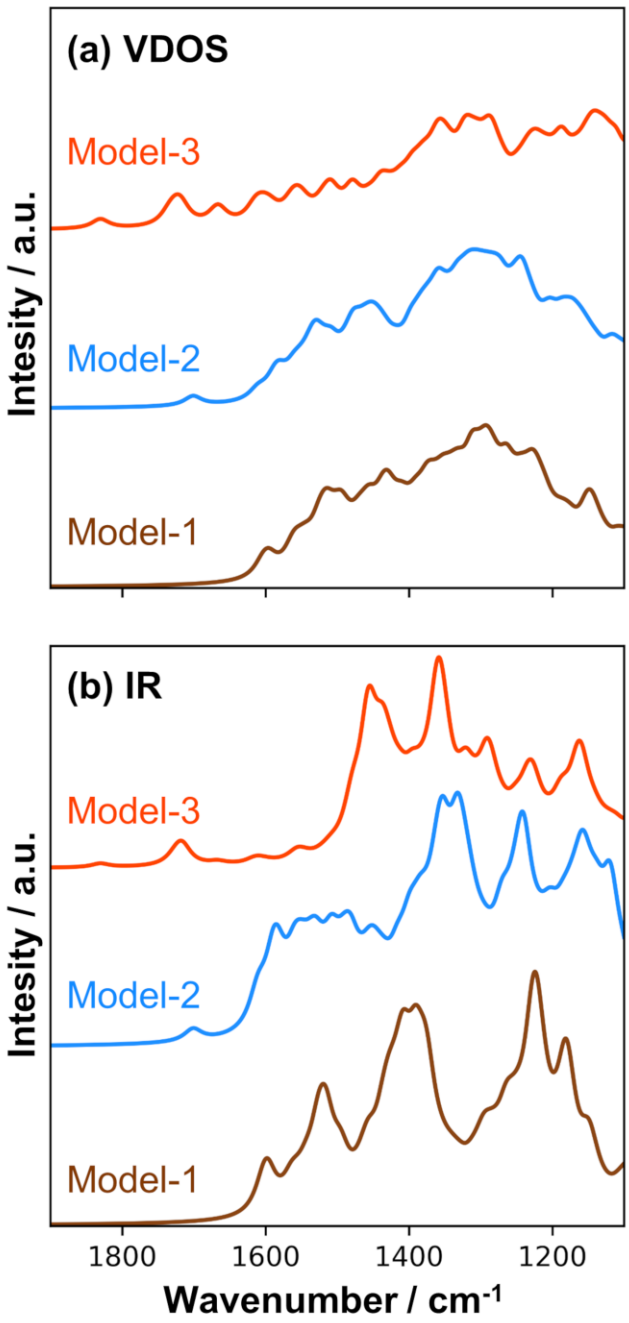

Figure S25. Computed VDOC and IR intensities of three rGO models. (**a**) Computed vibrational density of states (VDOS) for the three rGO models ($C_{114}O_{10}H_4$). (**b**) Computed Infrared (IR) intensities for the three rGO models. PBE functional is used for these calculations.

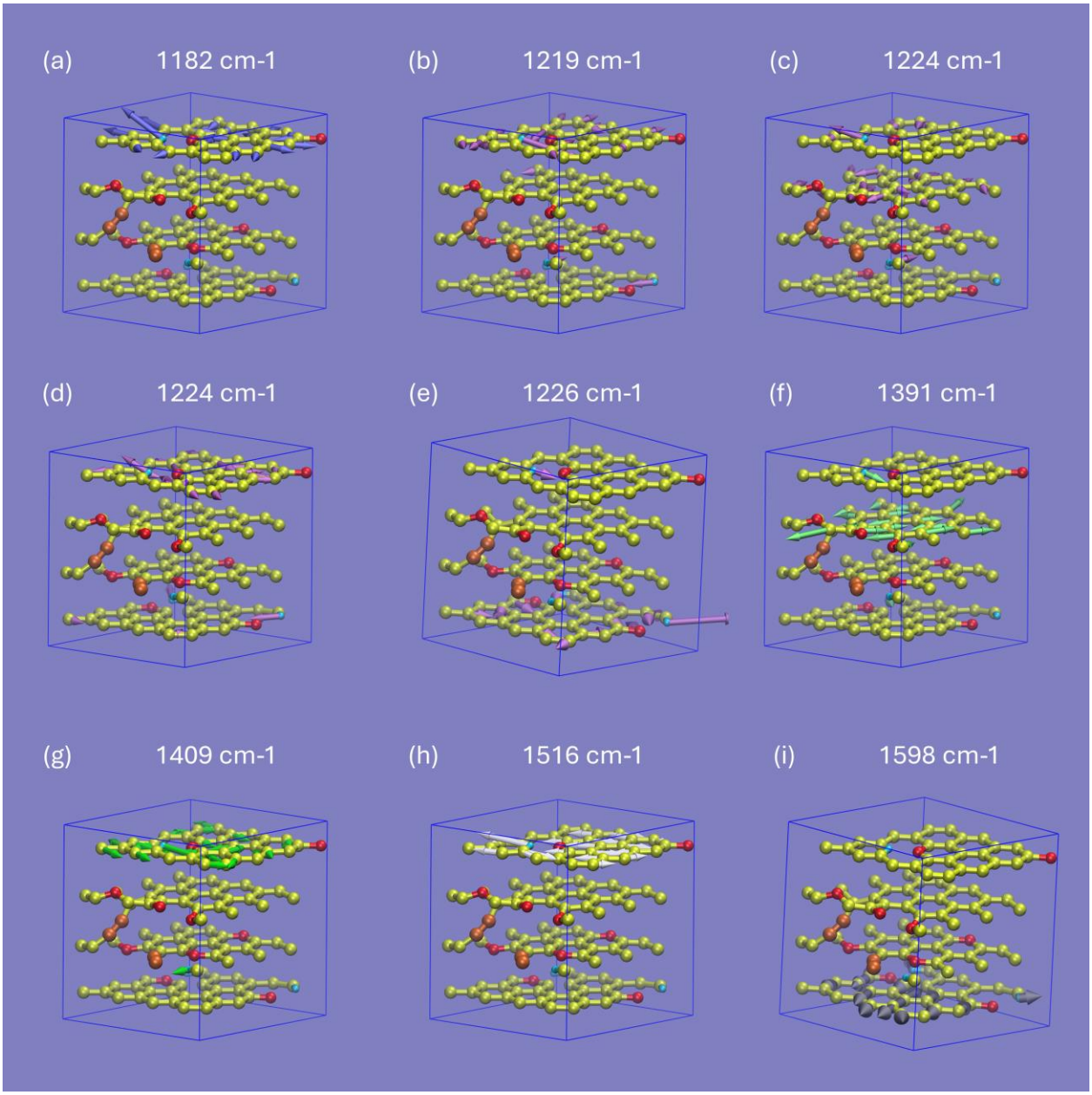

Figure S26. Various important normal modes contributing to the computed infrared (IR) peaks of the rGO Model-1. Note, the shown wavenumbers are the normal mode frequency and not the position of the peak intensity. (**a**) The IR peak at 1182 cm^{-1} (mode VI in **Table S9**) is attributed to this normal mode. (**b-e**) The IR peak at 1224 cm^{-1} (mode V in **Table-S9**) is attributed to these normal modes. (**f**) The IR peak at 1390 cm^{-1} (mode IV in **Table S9**) is attributed to this normal mode. (**g**) The IR peak at 1407 cm^{-1} (mode III in **Table S9**) is attributed to this normal mode. (**h**) The IR peak at 1519 cm^{-1} (mode II in **Table S9**) is attributed to this normal mode. (**i**) The IR peak at 1598 cm^{-1} (mode I in **Table S9**) is attributed to this normal mode.

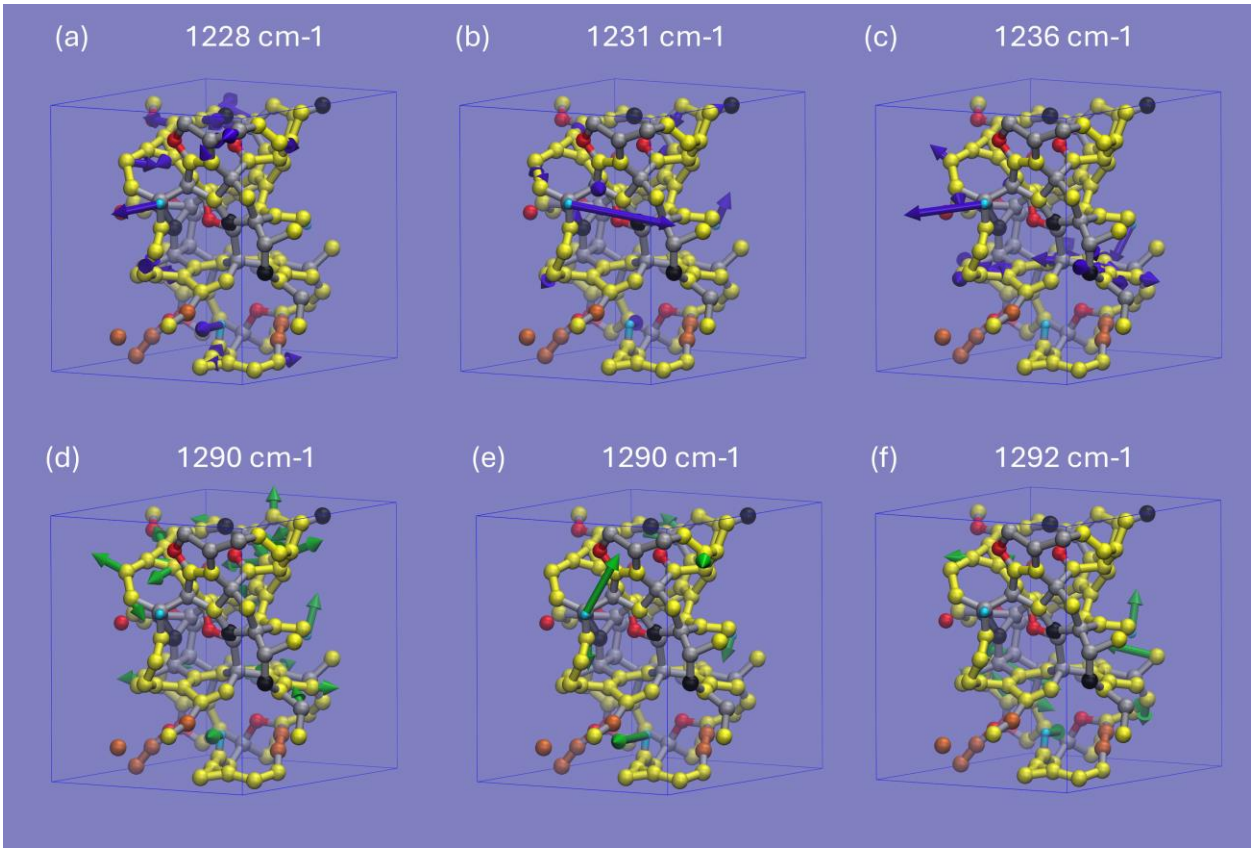

Figure S27. Various important normal modes contributing to the computed infrared (IR) peaks of the rGO Model-3. Note, the shown wavenumbers are the normal mode frequency and not the position of the peak intensity. (**a-c**) The IR peak at 1231 cm^{-1} is attributed to these normal modes. (**d-e**) The IR peak at 1291 cm^{-1} is attributed to these normal modes.

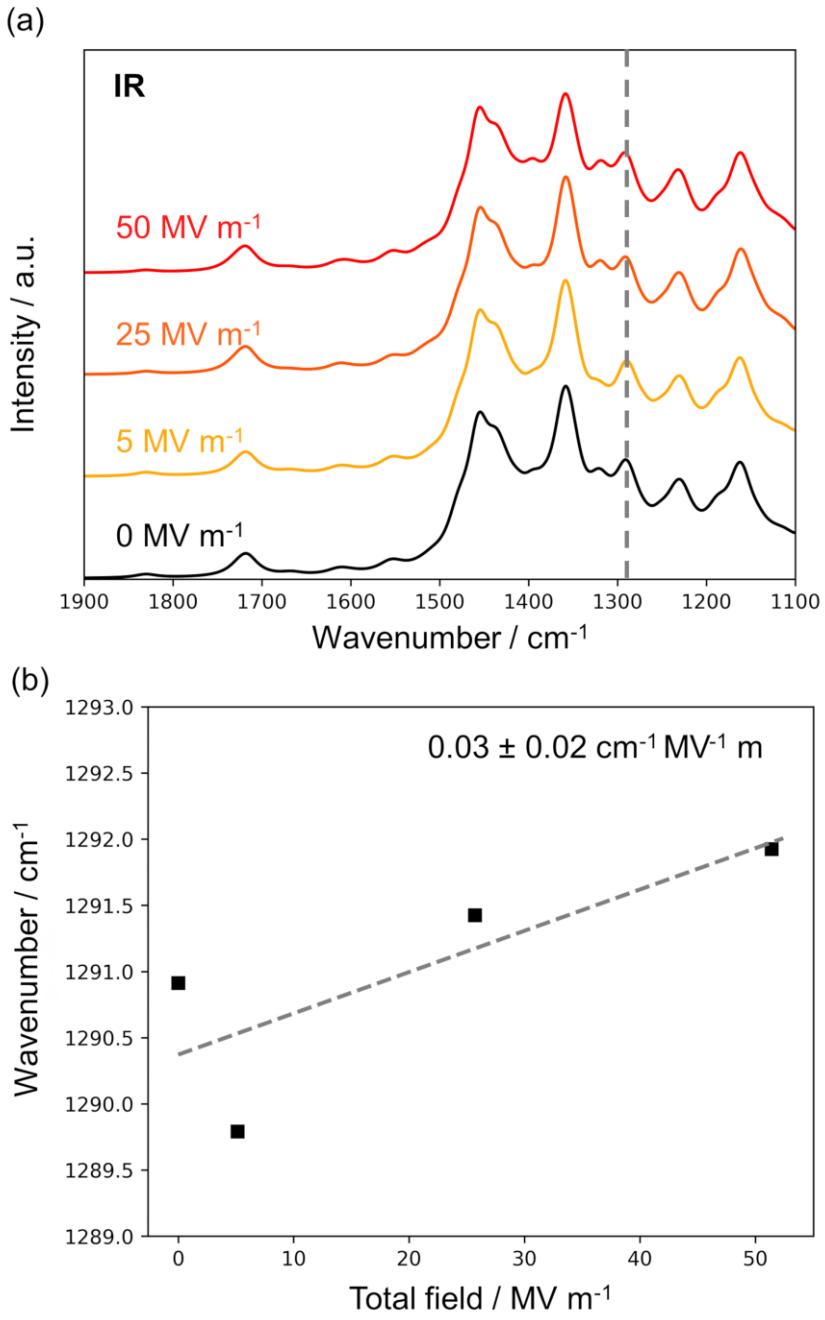

Figure S28. Effect of the application of finite total electric field along the z-direction on the IR spectra of rGO Model-3. Panel (**a**) shows the spectra, whereas panel **(b)** shows the shift of peak appearing at 1291 cm^{-1} due to the electric field.

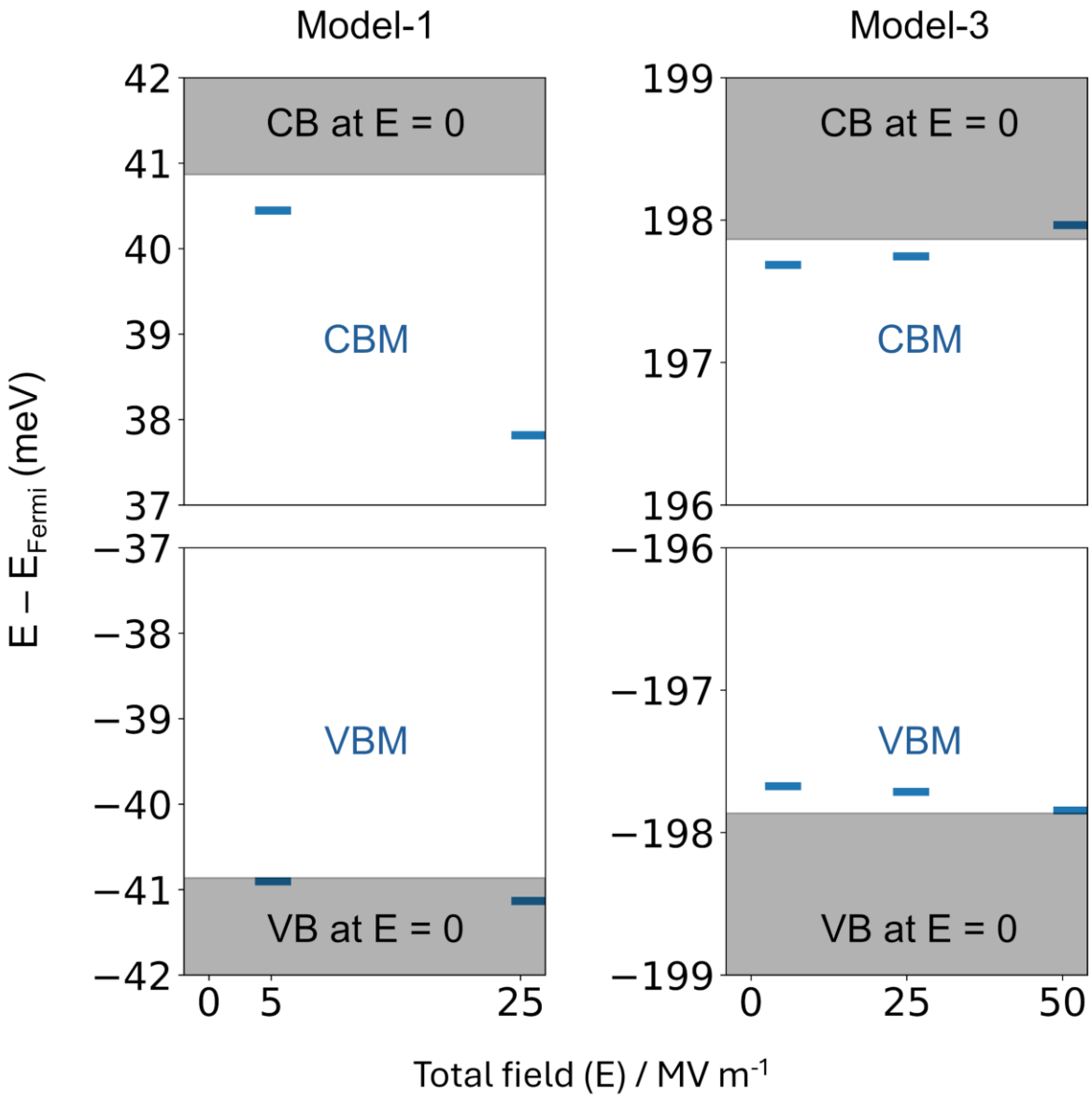

Figure S29. Position of valence band maximum and conduction band minimum compared in the presence and absence of a finite total electric field of two rGO models. The position of valence band maximum and conduction band minimum (VBM and CBM, respectively, shown with blue lines) in the presence of a finite total electric field (E) along the z-direction are compared with the valence and conduction band (VB and CB, respectively shown with gray shaded area) of Model-1 and Model-3 when no total electric field is present.

References

[1] M. Yaguchi, T. Uchida, K. Motobayashi, M. Osawa, *J. Phys. Chem. Lett.* **2016**, *7*, 3097–3102.
[2] A. Wuttig, J. Ryu, Y. Surendranath, *J. Phy. Chem. C* **2021**, *125*, 17042–17050.
[3] H. Ö. Doğan, D. Ekinci, Ü. Demir, *Surf. Sci.* **2013**, *611*, 54–59.
[4] F. Risplendi, M. Bernardi, G. Cicero, J. C. Grossman, *Appl Phys Lett* **2014**, *105*, 043903.
[5] A. Kundu, Y. Song, G. Galli, *Proc. Natl. Acad. Sci.* **2022**, *119*, e2203083119.
[6] F. Gygi, *IBM J. Re.s Dev.* **2008**, *52*, 137–144.
[7] J. P. Perdew, A. Zunger, *Phys. Rev. B* **1981**, *23*, 5048–5079.
[8] M. Schlipf, F. Gygi, *Comput Phys. Commun.* **2015**, *196*, 36–44.
[9] G. Bussi, D. Donadio, M. Parrinello, *J. Chem. Phys.* **2007**, *126*, 014101.
[10] J. P. Perdew, K. Burke, M. Ernzerhof, *Phys. Rev. Lett.* **1996**, *77*, 3865–3868.
[11] H. Huang, Z. Li, J. She, W. Wang, *J. Appl. Phys.* **2012**, *111*, 054317.
[12] N. Marzari, A. A. Mostofi, J. R. Yates, I. Souza, D. Vanderbilt, *Rev. Mod. Phys.* **2012**, *84*, 1419–1475.
[13] M. Stengel, N. A. Spaldin, *Phys. Rev. B.* **2006**, *73*, 075121.
[14] A. Kundu, M. Govoni, H. Yang, M. Ceriotti, F. Gygi, G. Galli, *Phys. Rev. Mater.* **2021**, *5*, L070801.
[15] A. Kundu, G. Galli, *J. Chem. Theory. Comput.* **2023**, *19*, 4011–4022.
[16] A. Kundu, "PyEPFD: a Python library for computing Electron-Phonon renormalizations from Finite Displacements," can be found under https://pyepfd.readthedocs.io/en/latest/, **n.d.**
[17] G. Piccini, J. Sauer, *J. Chem. Theory Comput.* **2013**, *9*, 5038–5045.
[18] A. Kundu, G. Piccini, K. Sillar, J. Sauer, *J. Am. Chem. Soc.* **2016**, *138*, 14047–14056.
[19] P. Norman, K. Ruud, T. Saue, *Principles and Practices of Molecular Properties: Theory, Modeling, and Simulations.*, John Wiley & Sons Ltd, **2018**.
[20] N. A. Spaldin, *J. Solid State Chem.* **2012**, *195*, 2–10.
[21] I. Souza, J. Íñiguez, D. Vanderbilt, *Phys. Rev. Lett.* **2002**, *89*, 117602.
[22] M. Acik, G. Lee, C. Mattevi, M. Chhowalla, K. Cho, Y. J. Chabal, *Nat. Mater.* **2010**, *9*, 840–845.
[23] M. Acik, G. Lee, C. Mattevi, A. Pirkle, R. M. Wallace, M. Chhowalla, K. Cho, Y. Chabal, *J. Phys. Chem. C* **2011**, *115*, 19761–19781.
[24] C. Zhang, D. M. Dabbs, L. M. Liu, I. A. Aksay, R. Car, A. Selloni, *J. Phys. Chem. C* **2015**, *119*, 18167–18176.
[25] J. W. Medernach, in *Handbook of Vibrational Spectroscopy* (Ed.: P.R. Griffiths), Wiley, **2001**.
[26] C. Vigano, J. Ruysschaert, E. Goormaghtigh, *Talanta* **2005**, *65*, 1132–1142.
[27] E. Karabudak, E. Yüce, S. Schlautmann, O. Hansen, G. Mul, H. (J. G. E.) Gardeniers, *Phys. Chem. Chem. Phys.* **2012**, *14*, 10882.
[28] T. Seki, K. Y. Chiang, C. C. Yu, X. Yu, M. Okuno, J. Hunger, Y. Nagata, M. Bonn, *J. Phys. Chem. Lett.* **2020**, *11*, 8459–8469.
[29] D. Enders, T. Nagao, T. Nakayama, M. Aono, *Langmuir* **2007**, *23*, 6119–6125.
[30] H. L. Guo, X. F. Wang, Q. Y. Qian, F. Bin Wang, X. H. Xia, *ACS Nano* **2009**, *3*, 2653–2659.
[31] B. Konkena, S. Vasudevan, *J. Phys. Chem. Lett.* **2012**, *3*, 867–872.

[32] E. S. Orth, J. G. L. Ferreira, J. E. S. Fonsaca, S. F. Blaskievicz, S. H. Domingues, A. Dasgupta, M. Terrones, A. J. G. Zarbin, *J. Colloid Interface Sci.* **2016**, *467*, 239–244.
[33] E. Toral-Sánchez, J. A. Ascacio Valdés, C. N. Aguilar, F. J. Cervantes, J. R. Rangel-Mendez, *Carbon* **2016**, *99*, 456–465.
[34] Y. Yamada, H. Yasuda, K. Murota, M. Nakamura, T. Sodesawa, S. Sato, *J. Mater. Sci.* **2013**, *48*, 8171–8198.
[35] R. Al-Gaashani, A. Najjar, Y. Zakaria, S. Mansour, M. A. Atieh, *Ceram. Int.* **2019**, *45*, 14439–14448.
[36] S. Yumitori, *J. Mater. Sci.* **2000**, *35*, 139–146.
[37] C. Mattevi, G. Eda, S. Agnoli, S. Miller, K. A. Mkhoyan, O. Celik, D. Mastrogiovanni, G. Granozzi, E. Carfunkel, M. Chhowalla, *Adv. Funct. Mater.* **2009**, *19*, 2577–2583.
[38] D. Joung, S. I. Khondaker, *J. Phys. Chem. C* **2013**, *117*, 26776–26782.
[39] D. D'Angelo, C. Bongiorno, M. Amato, I. Deretzis, A. La Magna, E. Fazio, S. Scalese, *J. Phys. Chem. C* **2017**, *121*, 5408–5414.
[40] M. Osawa, M. Ikeda, *J. Phys. Chem.* **1991**, *95*, 9914–9919.
[41] J. Prashanth, J. K. Ojha, B. V. Reddy, G. R. Rao, *J. Phys. Conf. Ser.* **2016**, *759*, 012057.
[42] M. Osawa, K. Ataka, K. Yoshii, T. Yotsuyanagi, *J. Electron. Spectros. Relat. Phenomena* **1993**, *64–65*, 371–379.
[43] M. Osawa, *Bull. Chem. Soc. Jpn.* **1997**, *70*, 2861–2880.
[44] M. Osawa, in *Diffraction and Spectroscopic Methods in Electrochemistry (Advances in Electrochemical Science and Engineering, Vol.9)* (Eds.: R.C. Alkire, D.M. Kolb, J. Lipkowski, P.N. Ross), Wiley-VCH, New York, **2006**, pp. 269–314.
[45] F. Le, D. W. Brandl, Y. A. Urzhumov, H. Wang, J. Kundu, N. J. Halas, J. Aizpurua, P. Nordlander, *ACS Nano* **2008**, *2*, 707–718.
[46] X. Yang, Z. Sun, T. Low, H. Hu, X. Guo, F. J. García de Abajo, P. Avouris, Q. Dai, *Adv. Mater.* **2018**, *30*, 1704896.
[47] G. Samjeské, A. Miki, S. Ye, M. Osawa, *J. Phys. Chem. B* **2006**, *110*, 16559–16566.
[48] G. Samjeské, A. Miki, M. Osawa, *J. Phys. Chem. C* **2007**, *111*, 15074–15083.
[49] M. Osawa, in *In-Situ Spectroscopic Studies of Adsorption at the Electrode and Electrocatalysis*, Elsevier, **2007**, pp. 209–246.
[50] H. Miyake, T. Okada, G. Samjeské, M. Osawa, *Phy. Chem. Chem. Phys.* **2008**, *10*, 3662.